Provided by the author(s) and University of Galway in accordance with publisher policies. Please cite the published version when available.

Title	An experimental and kinetic modeling study of the pyrolysis and oxidation of n-C-3-C-5 aldehydes in shock tubes
Author(s)	Pellucci, Matteo; Somers, Kieran P.; Yasunaga, Kenji; Burke, Ultan; Alessio, Frassoldati; Ranzi, Eliseo; Curran, Henry J.; Faravelli, Tiziano
Publication Date	2015-08-24
Publication Information	Pelucchi, M,Somers, KP,Yasunaga, K,Burke, U,Frassoldati, A,Ranzi, E,Curran, HJ,Faravelli, T (2015) 'An experimental and kinetic modeling study of the pyrolysis and oxidation of n-C-3-C-5 aldehydes in shock tubes'. Combustion And Flame, 162 :265-286.
Publisher	Elsevier ScienceDirect
Link to publisher's version	http://dx.doi.org/10.1016/j.combustflame.2014.07.027
Item record	http://hdl.handle.net/10379/6122
DOI	http://dx.doi.org/10.1016/j.combustflame.2014.07.027

Downloaded 2024-03-13T07:31:16Z

Some rights reserved. For more information, please see the item record link above.

An experimental and kinetic modeling study of the pyrolysis and oxidation of *n*-C_3–C_5 aldehydes in shock tube

Keywords

aldehydes, shock tube, kinetic modeling, ignition, pyrolysis

Abstract

Due to the increasing interest in the use of biofuels for energy production, it is of great importance to better understand the combustion and thermal decomposition characteristics of species such as aldehydes. These are known to be key intermediate products of transport bio-fuels combustion and are also dangerous pollutants emitted from combustion in internal combustion engines and from gasification of biomasses. In this study, an experimental and kinetic modeling investigation of propanal, *n*-butanal and *n*-pentanal oxidation and pyrolysis in two shock tube facilities was carried out. Ignition delay times for mixtures of pure propanal/*n*-butanal/*n*-pentanal (1%)–O_2/Ar were measured in the temperature range 1087–1847 K, at pressures of 1 and 3 atm, and at equivalence ratios of 0.5, 1.0 and 2.0. Additional experiments were carried out in a single pulse shock tube to determine the speciation profiles of the fuels and intermediate species under pyrolysis conditions for mixture of pure propanal/*n*-butanal/*n*-pentanal (3%)–Ar (97%), at averaged reflected pressure of 1.9 atm and at reflected shock temperatures of 972–1372 K.

A comprehensive sub-mechanism for the high temperature kinetics of the three aldehydes was developed. This scheme was then coupled with NUIG (National University of Ireland, Galway) and POLIMI (Politecnico di Milano) kinetic schemes. Both of the models were validated and showed good agreement with the new experimental data. The mechanisms are also compared with available literature ignition delay times, speciation profiles and laminar burning velocities with reasonable agreement observed. Reaction pathways and sensitivity analyses were also performed to highlight the important reaction steps involved in the pyrolysis and oxidation processes. The apparent activation energies of experimental and predicted ignition delay times are also discussed, giving insights into experimental uncertainties, but mainly highlighting the relevant role of the C_0–C_4 sub-mechanism in characterizing the auto-ignition behavior of combustion systems. Recommendations for future studies are also made.

1. Introduction

The depletion of fossil fuel reserves and the stringent targets for air pollution reduction have largely increased the focus on gaseous, liquid and solid biofuels as a sustainable source of energy for transport, domestic and industrial applications. Biomasses can be used to produce either liquid or gaseous biofuels for transportation purposes (hydrogen, methane, ethanol and long chain alcohol, dimethyl ether, diesel) through different processes such as Biomass-To-Liquid (BTL) or as a side product of Gas-To-Liquid (GTL) processes in Fischer-Tropsch synthesis. Similarly, municipal solid waste (MSW), agricultural and forest residues can also be converted to feedstock for energy production through gasification or combustion, followed by conventional power generation cycles.

Within this scenario, low and high molecular weight aldehydes are known to be toxic, some of them carcinogenic, and precursors of free radicals leading to the formation of ozone and urban smog [1].

C_4 and C_5 aldehydes belong to the class of non-regulated pollutants and they are classified as mobile source air toxic (MSAT) compounds. They are products of partial or incomplete combustion and are released into the atmosphere from conventional spark ignition (SI) gasoline and compression ignition (CI) diesel engines, and also from biomass gasification or aerobic treatments [2]. Grosjean *et al.* [3] studied carbonyl emissions from light-duty and heavy-duty vehicles on a motorway tunnel, detecting emissions of saturated, unsaturated and aromatic aldehydes. Zervas [4] analyzed the exhaust gases from a diesel engine recording high emission of carbonyl compounds, particularly when synthetic fuels were tested compared to a commercial fuel. Karavalakis *et al.* [5] highlighted how the use of a Euro4 engine increases the emissions (aldehydes and ketones) compared to a Euro3 engine identifying linear aldehydes from formaldehyde up to C_5–C_6 and aromatic aldehydes. De Abrantes and co-workers focused on formaldehyde and acetaldehyde emissions from diesel engines [6], highlighting higher concentrations than those observed in spark ignition engines. Gasoline and diesel engine emissions of aldehydes were also compared by Roy [7] through high performance liquid chromatography. Significant and comparable amounts of formaldehyde, acetaldehyde and propanal were detected from SI and CI engines investigating different injection technologies. Schauer [8] measured the emissions of aldehydes from a gasoline-powered vehicle, detecting concentrations in the order of those measured for diesel engines. Other works in recent years focused on the influence of diesel-biodiesel blended fuels on carbonyl emissions, agreeing that alternative fuel blending increases the release of aldehydes and that the engine technology influences the phenomena as much as the kind of fuel blend itself [9–13].

From a pure chemical kinetics perspective aldehydes are primary stable intermediate products of biofuel oxidation and pyrolysis, influencing reaction pathways and important combustion properties [14]. Therefore their combustion behavior is non-negligible with respect to designing more efficient and environmentally friendly combustion systems. For all of these reasons, the understanding of combustion kinetics of aldehydes and furthermore a deeper understanding of the reactivity of the carbonyl side of the molecule (R–CH=O) under combustion or pyrolytic conditions, play a crucial role in the capability of kinetic mechanisms to better predict pollutant release from both conventional and renewable fuels.

Recent fundamental studies of biofuel combustion have addressed the strong belief that long-chain alcohols (propanol, butanol, pentanol and related isomers) are likely to be used as an alternative to conventional gasoline (*n*-butanol and *iso*-pentanol mainly) either as additives in order to reduce pollution in terms of PAH, particulates and soot formation. Fundamental studies on the oxidation of alcohols identified the presence of aldehydes as intermediate products derived from radical as well as molecular dehydrogenation reactions [15–28].

Since the pioneering work of Dean and co-workers [29] and of Hochgreb and Dryer [30], several kinetic studies on the pyrolysis and oxidation of formaldehyde at low- and high-temperature were undertaken [31–35].

Similarly, acetaldehyde oxidation has been described in detail by different authors. Dating back to the early 1970s Halstead *et al.* [36] discussed cool flames phenomena and low-temperature oxidation. Oscillatory ignitions in the low-temperature regime were studied in the early 80s by Gray and co-workers [37], and in the 90s by Cavanagh [38] and by Di Maio *et al.* [39]. Kaiser proposed a model to describe the negative temperature coefficient (NTC) behavior of acetaldehyde [40]. The high-temperature oxidation of acetaldehyde was investigated by Dagaut [41] in a jet-stirred reactor and in a shock tube, while Hidaka and co-workers studied its pyrolysis in a single-pulse shock tube [42], and Yasunaga suggested a mechanism describing the oxidation and pyrolysis for the high-temperature regime [43].

Kaiser [44] developed a chemical kinetic model to describe propanal oxidation in the temperature range 400–700 K. An experimental and modeling study at higher temperatures was carried out by Lifshitz and co-workers [45]. They investigated the thermal decomposition of propanal in a single pulse shock-tube under pyrolysis conditions. A sub-mechanism of 52 elementary reaction steps and 22 species was developed, and the kinetic analysis emphasized the importance of unimolecular initiation reactions involving a C–C bond breaking in predicting the intermediate and product species. Furthermore, the species profile predictions were found to be sensitive to the ratio between abstraction by ethyl radical on the fuel molecule and ethyl radical decomposition to form ethylene and a hydrogen atom. Kasper *et al.* [46] studied the combustion chemistry of propanal in a stoichiometric flame at low pressures with molecular beam mass spectrometry, highlighting the importance of alkyl radical addition to the fuel molecule and the need of more detailed kinetic studies to assess the relative importance of available reaction pathways. Akih-Kumgeh and Bergthorson [47] studied the ignition of propanal in a shock tube and developed a mechanisms underlining the importance of the initiation reaction forming $\dot{C}_2H_5$ and $H\dot{C}O$ and the H-atom abstraction reactions from the alpha-carbonyl site in predicting ignition delay times. Laminar flame speeds were measured by Veloo *et al.* [48] together with jet-stirred reactor experiments to quantify reactant, intermediate and product concentrations. A model to describe the low- and high-temperature oxidation of propanal was then developed and validated.

Veloo and co-workers also studied *n*-butanal and *iso*-butanal oxidation in laminar flames and in a jet-stirred reactor proposing a comprehensive mechanism for low- and high-temperature combustion consisting of 244 species and 1198 elementary reaction steps [49]. The authors highlighted the importance of $\dot{C}_3H_5$ radical distribution and other key reaction subsets of the mechanism. An interesting comparison between *n*- and *iso*-butanal and propanal is also shown for flame speed data, with an emphasis on radical species profiles such as $H\dot{C}O$ and $\dot{O}H$ being of high importance in flame propagation phenomena. Davidson and co-workers investigated the ignition behavior of *n*-butanal [50] as part of an update to the Dooley *et al.* methyl butanoate mechanism [51]. Zhang measured ignition delay times for *n*-butanal [52] and *i*-butanal [53] over a wide range of equivalence ratios, pressures and temperatures, and developed kinetic sub-models for both of the C_4 aldehydes based on a literature review and validated them against the measured data.

Da Silva and Bozzelli [54] calculated the enthalpies of formation of C_2 to C_7 *n*-aldehydes through ab initio calculations and determined bond dissociation energies (BDE) for all C–C and C–H bonds in the molecules. Their study revealed that the $R–CH_2CH=O$ bond is the weakest bond in all the aldehydes larger than acetaldehyde, due to the formation of the resonantly stabilized vinoxy radical. To the best of our knowledge no studies currently exist for *n*-butanal and *n*-pentanal pyrolysis, and furthermore no kinetic mechanisms are available in the literature to describe *n*-pentanal oxidation.

There have clearly been significant efforts focused on understanding the combustion behavior of aldehydes. Yet a consistent and detailed summary of their combustion behavior is still somewhat lacking in the literature.

Two important goals support and justify the present work. Firstly, it provides new experimental data on the pyrolysis and the auto-ignition behavior of C_3–C_5 aldehydes, in order to extend the database available for high-temperature combustion conditions. Secondly, the experimental data, both from the current study and from the literature, have been used to develop and validate the sub-mechanism of C_3–C_5 aldehydes, with the objective of better characterizing the role of the acyl group. This validation has been performed by coupling a newly developed aldehyde sub-mechanism with the C_0–C_4 mechanism of NUIG [55–60] and the one of POLIMI [61]. In an attempt to gain an optimal overall agreement with experimental data in the overall range of operating conditions, self-consistency has been preserved within each mechanism, in line with previous studies from both groups.

Both of the mechanisms were previously validated for formaldehyde and acetaldehyde. Figure 1 shows a first comparison of both of the mechanisms with experimental data. Figure 1a shows the oxidation of formaldehyde in an atmospheric pressure flow reactor at 1095 K and $\varphi = 1.08$ [31], while figure 1b shows the high-temperature pyrolysis of acetaldehyde in a shock tube [43]. Figure 2 compares the ignition delay times of formaldehyde [34] and acetaldehyde [43] (1% fuel in oxygen-argon) at lean conditions ($\varphi = 0.5$). The higher reactivity of formaldehyde is evident in this figure, mainly at lower temperatures. The apparent activation energies are significantly different, in the order of 40 kcal mol^{-1} for formaldehyde and close to 60 kcal mol^{-1} for acetaldehyde. At temperatures higher than 1600 K, both aldehydes have similar reactivity. These comparisons show that both of the models agree with the experimental data, providing a solid basis for the development of kinetic mechanisms for heavier aldehydes.

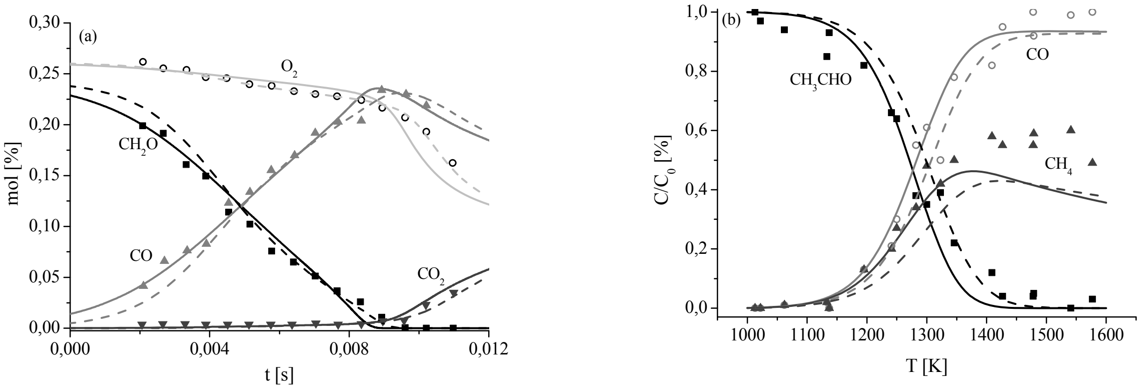

Figure 1: a) Oxidation of formaldehyde at 1 atm and 1095 K [31]. b) Pyrolysis of acetaldehyde at 2 atm and 2 ms residence time [43]. Comparison of experimental data (symbols) and predictions of NUIG (dashed lines) and POLIMI (solid lines) kinetic schemes.

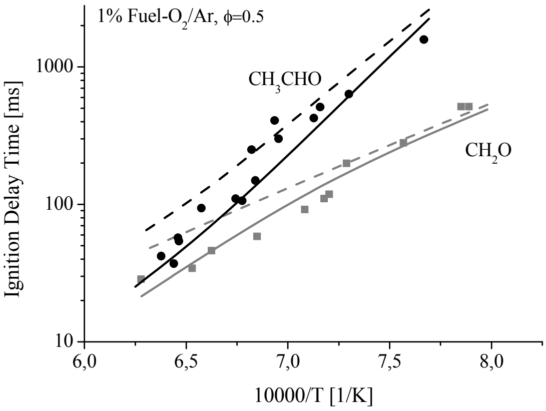

Figure 2: Ignition delay times of formaldehyde [34] and acetaldehyde [43] oxidation. Comparison of experimental data (symbols) and predictions of NUIG (dashed lines) and POLIMI (solid lines) kinetic schemes.

2. Experimental Approach

Two shock tubes were used in this study, the first one at the National Defense Academy in Japan to study the pyrolysis of *n*-butanal and *n*-pentanal. The second one, at the National University of Ireland Galway (NUIG), was used to measure ignition delay times of propanal, *n*-butanal and *n*-pentanal at different oxidation conditions.

2.1 Pyrolysis

The pyrolysis experiments of propanal, *n*-butanal and *n*-pentanal were performed in a single-pulse magic-hole type shock tube (SPST) (Hidaka *et al.* [62–65]). The experimental conditions studied are summarized in Table 2.

The reacted gas mixtures, quenched using the single-pulse method, were extracted into a pre-evacuated vessel (50 cm^3) through a valve near the end-plate. The reacted gas mixtures were analyzed by three serially connected gas chromatographs equipped with thermal conductivity detectors (TCD) [64, 65].

Aldehyde	**Fuel [%]**	**Ar [%]**	T_{range} **[K]**	p **[atm]**	t_e/ms
propanal	3.00	97.00	1013–1356	1.8±0.3	2.6±0.5
***n*-butanal**	3.00	97.00	1096–1368	1.9±0.5	1.9±0.5
***n*-pentanal**	3.00	97.00	972–1372	2.1±0.4	2.3±0.5

Table 1: Summary of experimental work carried out in the SPST at the National Defense Academy, Japan.

Shimadzu GC-8APT with Helium as carrier gas, equipped with different columns, was used for the different analysis in the post-shock mixtures:

- a 2m column packed with Sebaconitrile and heated to 348 K to detect propanal
- a 2 m column of Porapak Q coupled with a 2 m column of Unibeads 1S to determine C_2 and C_3 hydrocarbons
- a 2 m column of Molecular Sieve 5A at 323 K to determine methane and CO.

According to Hidaka *et al.* [63, 64], an effective reaction time (t_e) was defined as the time between the heating of the mixture by the reflected shock wave and the time at which the reflected shock pressure had fallen by 20%. Assuming the adiabatic expansion of a non-reactive mixture, the temperature drops by ≈ 8.5% from its initial value at t_e. Given that the single-pulse shock tube has cooling rates of 6.6×10^5 K s^{-1} [62], it can be assumed that the reaction was frozen at t_e. The validity of the effective heating time and cooling rate was previously tested for N_2O pyrolysis [62].

The uncertainty in the measured concentration of small hydrocarbons in the post-shock mixtures is less than 2%, except for fuels where the estimate uncertainty is less than 30%. The uncertainty in the reaction time is 5% and in the reflected shock temperature is ±1%. Maximum uncertainties in the reflected pressure are ±0.5 atm based on the standard deviation (σ) of our experiments, while those in the residence time are ±0.5 ms.

2.2 Ignition Delay Times

The shock tube based at NUI Galway, a standard type UV Emission Shock Tube (UEST), was previously described in detail by Smith *et al.* [66] and will be briefly discussed here. It consists of a test section measuring 6.22 m in length with an internal diameter of 10.24 cm and a barrel-shaped driver section measuring 53 cm in length. The two sections are separated by a polycarbonate diaphragm which bursts when forced into contact with a cross-shaped cutter due to the pressure differential. Four pressure transducers located along the last half meter of the test section were used to determine the velocity of the incident shock wave. The velocity at the end-plate was determined via linear extrapolation, taking shock wave attenuation into account. The Gaseq [67] equilibrium program was used to determine the reflected shock parameters from the known initial temperature, mixture pressure and incident shock velocity *via* the usual one-dimensional equations.

The pressure at the end-plate was recorded using a pressure transducer (Kistler, model 603B). Light emission at 431 nm from excited CH* radical was detected through a fused silica window embedded in the end-plate using a photo-detector (Thorlabs Inc. PDA55-EC) and a narrow band-pass filter centered at 430 nm, with a full width half-maximum of 10 nm. The ignition delay time was defined as the time interval between the rise in pressure due to the arrival of the shock wave at the end-plate and the extrapolation of the maximum slope of CH* emission to the zero signal level as reported in Figure 3.

Propanal (97.0% pure) was supplied by Sigma-Aldrich while *n*-butanal (99.0%) and *n*-pentanal (97.0%) were supplied by TCI Europe. Fuels were degassed before being introduced into the mixing tanks by a series of freeze-pump-thaw cycles until no gas was observed to escape from the fuel as the solid thawed. Oxygen (99.5%) and argon (99.998%) were provided by BOC Ltd and were introduced in the mixing tanks through the manifolds from gas cylinders. For each aldehyde, 1% fuel mixtures were prepared at three different equivalence ratios (φ = 0.5, 1.0 and 2.0) using the method of partial pressures and their composition are provided in Table 2, together with the temperatures and pressures measured for each mixture. We estimate an uncertainty of ±0.10 and ±0.25 atm in the reflected shock pressure, respectively for 1 and 3 atm experiments, based on the standard deviation (σ) of the data. Uncertainties of 1% are present in the reflected shock temperature. An uncertainty of 15% is estimated in the ignition delay time of each experiment due to uncertainties in the condition behind the reflected shock wave. Uncertainties in the mole fractions of reactants are minimal (<5%) as high accuracy digital pressure gauges were used in the preparation of the mixture.

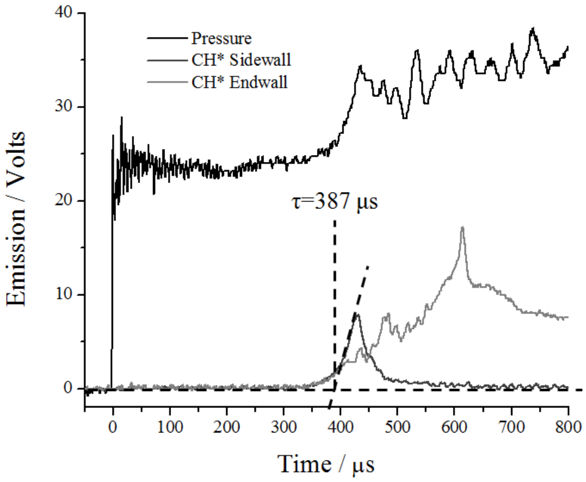

Figure 3: End-wall pressure trace and $\mathrm{CH}^{\star}$ chemiluminescence measurements with corresponding ignition delay time,

1% *n*-butanal, 5.5% O_2, 93.5% Ar, p = 1.2 atm, T = 1349.1 K.

Fuel	φ	Fuel [%]	O_2 [%]	Ar [%]	T_5 [K]	p [atm]
propanal	0.5	1.00	8.00	91.00	1136–1405 1170–1336	1.25±0.08 2.49±0.13
	1.0	1.00	4.00	95.00	1171–1612 1201–1479	1.22±0.12 2.75±0.25
	2.0	1.00	2.00	97.00	1358–1747 1302–1598	1.21±0.09 2.91±0.30
***n*-butanal**	0.5	1.00	11.00	88.00	1232–1495 1224–1424	1.10±0.06 3.14±0.11
	1.0	1.00	5.50	93.50	1303–1547 1271–1475	1.20±0.13 3.23±0.16
	2.0	1.00	2.75	96.25	1376–1740 1321–1610	1.07±0.05 2.84±0.17
***n*-pentanal**	0.5	1.00	14.00	85.00	1211–1447 1087–1338	0.98±0.05 3.01±0.33
	1.0	1.00	7.00	92.00	1226–1538 1181–1481	1.06±0.05 2.89±0.15
	2.0	1.00	3.50	95.50	1363–1847 1238–1592	1.08±0.07 3.16±0.11

Table 2: Summary of experimental work carried out in the low pressure shock tube at the National University of Ireland, Galway.

3. Kinetic Mechanism of Aldehydes

3.1 Thermochemistry

The thermodynamic data for the three aldehydes (Figure 4) and related radicals, were calculated using the THERM program from Ritter and Bozzelli [68], based on group additivity methods developed by Benson [69] and further optimized by Burke [58] at NUIG. The computed values of enthalpies, entropies of formation and heat capacities for aldehydes and primary radicals are shown in Table 3, together with enthalpies of formation computed by da Silva and Bozzelli [54], and the nomenclature used in this study. Good agreement between the group additivity rules and the theoretical computations is shown in Table 3, with maximum deviations being within 1.5–2.0 kcal mol^{-1} for the enthalpies of formation. The bond dissociation energies (BDE) for the three aldehydes will be analyzed in the next paragraph when discussing chain initiation reactions.

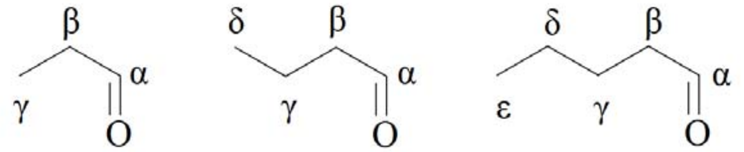

Figure 4: propanal, *n*-butanal and *n*-pentanal chemical structure and named carbon sites

Aldehyde and radical site	**Name**	**ΔH°$_f$ (298.15 K) [54]**	**ΔH°$_f$ (298.15 K) ***	**S°(298.15 K) ***	**C$_p$ (cal mol^{-1} K^{-1}) ***				
		(kcal mol^{-1})	**(kcal mol^{-1})**	**(cal mol^{-1}K^{-1})**	**300 K**	**500 K**	**800 K**	**1000 K**	**1500 K**
Propanal	C_2H_5CHO	–45.18	–45.35	72.86	19.38	26.94	36.90	42.12	49.83
α	$C_2H_5\dot{C}O$	–8.00	–8.45	73.98	18.55	24.98	33.74	38.39	45.19
β	$\dot{C}_2H_4CHO$-1	–7.10	–5.55	70.49	18.02	25.21	34.24	39.01	46.33
γ	$\dot{C}_2H_4CHO$-2	5.10	3.73	76.20	18.85	25.19	33.53	38.03	44.79
***n*-butanal**	*n*-C_3H_7CHO	–50.00	–50.31	82.28	24.82	35.26	48.21	54.29	64.57
α	*n*-$C_3H_7\dot{C}O$	–13.00	–13.41	83.40	23.99	33.30	45.05	50.56	59.93
β	$\dot{C}_3H_6CHO$-1	–11.50	–10.51	79.91	23.46	33.53	45.55	51.18	61.07
γ	$\dot{C}_3H_6CHO$-2	–2.50	–4.48	86.29	23.29	32.26	44.04	49.65	59.28
δ	$\dot{C}_3H_6CHO$-3	0.10	–1.23	85.62	24.29	33.51	44.84	50.20	59.53
***n*-pentanal**	*n*-C_4H_9CHO	–54.61	–55.27	91.70	30.26	43.58	59.52	66.46	79.31
α	*n*-$C_4H_9\dot{C}O$	–18.30	–18.37	92.82	29.43	41.62	56.36	62.73	74.67
β	$\dot{C}_4H_8CHO$-1	–17.20	–15.47	89.33	28.90	41.85	56.86	63.35	75.81
γ	$\dot{C}_4H_8CHO$-2	–8.10	–9.44	95.71	28.73	40.58	55.35	61.82	74.02
δ	$\dot{C}_4H_8CHO$-3	–7.60	–9.44	95.71	28.73	40.58	55.35	61.82	74.02
ε	$\dot{C}_4H_8CHO$-4	–5.20	–6.19	95.04	29.73	41.83	56.15	62.37	74.27

Table 3: Thermochemical data and nomenclature of aldehydes and related primary radicals (*group additivity).

3.2 Primary reactions of aldehydes

Figures 5–7 show simplified primary chain propagation reactions of the three aldehydes, in terms of initiation, H-atom abstraction, and radical decomposition reactions. The chain initiation reactions occur *via* unimolecular decompositions with a C–C bond cleavage, forming an alkyl radical and an oxygenated radical ($H\dot{C}O$, $\dot{C}H_2CHO$, $\dot{C}_2H_4CHO$-2, $\dot{C}_3H_6CHO$-3). At flame temperatures, the chain initiation and the reverse recombination reactions involving the C–H bonds can become significant.

H-atom abstraction reactions are reported in their general form with $\dot{R}$ being the generic H-atom abstracting radical. These reactions lead to three, four and five primary fuel radicals, respectively, for propanal, *n*-butanal and *n*-pentanal. Radical decomposition reactions proceed to form either an alkene and an oxygenated radical or an unsaturated oxygenated species (CO, ketene, acrolein, methylketene, or 1-butenal) and a small alkyl radical. For instance, the α-radical derived from the C_n aldehyde could, in principle, decompose via β-scission to form either ketene and a C_{n-2} alkyl radical or, more likely, CO and a C_{n-1} alkyl radical. Radicals can also isomerize mainly to form the thermodynamically favored α-radical. For the sake of clarity, isomerization pathways are not reported in Figures 3–5.

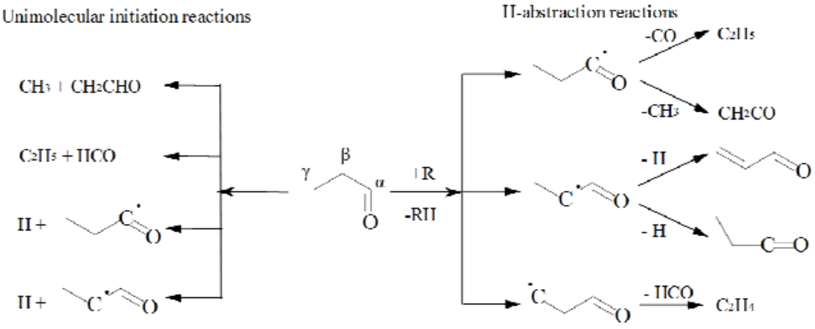
Unimolecular initiation reactions
H-abstraction reactions
$CH_3 + CH_2CHO$
$C_2H_5 + HCO$
H +
H +
γ
β
α
O
+R
-RH
-CO
C_2H_5
$-CH_3$
CH_2CO
- H
- H
O
C
- HCO
C_2H_4

Figure 5: Primary decomposition reactions of propanal.

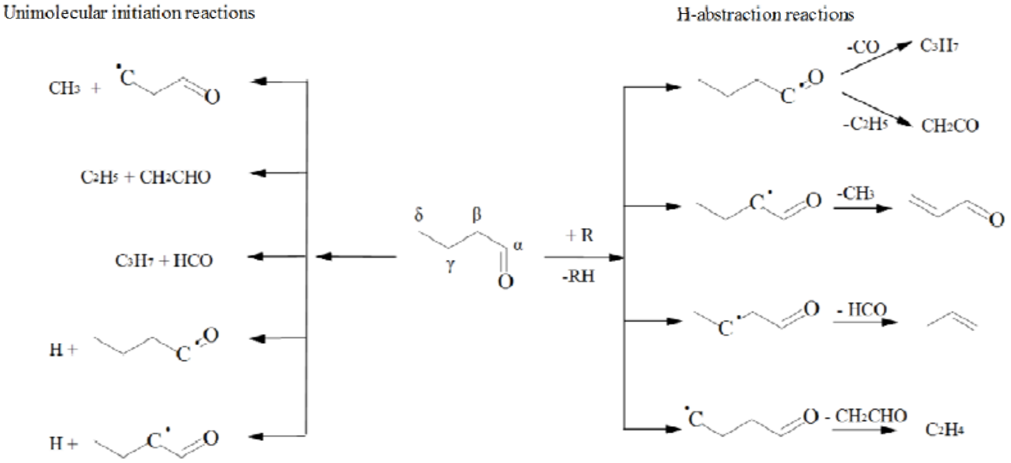
Unimolecular initiation reactions
H-abstraction reactions
CH_3 +
$C_2H_5 + CH_2CHO$
$C_3H_7 + HCO$
H +
H +
δ
β
γ
α
O
+ R
-RH
-CO
C_3H_7
$-C_2H_5$
CH_2CO
$-CH_3$
- HCO
$- CH_2CHO$
C_2H_4

Figure 6: Primary decomposition reactions of *n*-butanal.

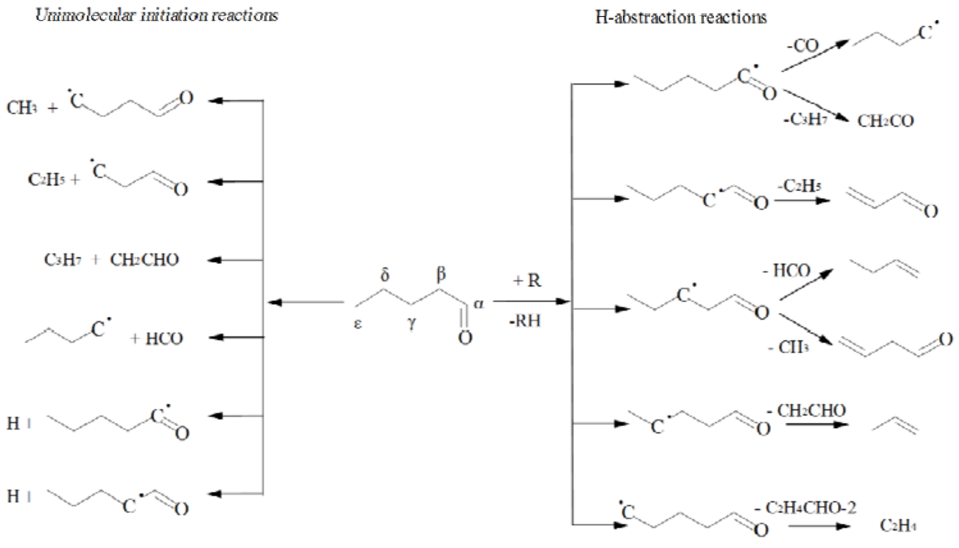

Figure 7: Primary decomposition reactions of *n*-pentanal.

3.2.1 Unimolecular Decomposition Reactions

A three-frequency version of Quantum-Rice-Ramsperger-Kassel theory (QRRK) [70–72] was used to calculate the temperature and pressure dependency of unimolecular decomposition reactions involving the three aldehydes. Collisional stabilization was calculated using a modified strong collision approximation. The high-pressure limiting rate constants were calculated through microscopic reversibility using estimates for radical-radical recombination reactions. Table 4 shows the resulting BDE compared to those evaluated by da Silva and Bozzelli [54]. The C_β–C_γ is the weakest bond, as would be expected from the proximity to the electron withdrawing carbonyl group, followed by C_α–C_β. The weakest C–H bond is the C_α–H, followed by C_β–H. Once again group additivity methods show good agreement with theoretical computations.

Bond	propanal		*n*-butanal		*n*-pentanal	
	This work	[54]	This work	[54]	This work	[54]
C_α–C_β	84.4	83.8	84.6	84.1	84.5	83.4
C_β–C_γ	83.5	83.7	82.3	82.5	82.5	82.3
C_γ–C_δ			89.1	90.1	87.9	88.5
C_δ–C_ε					89.1	89.4
C_α–H	89.0	89.3	89.0	89.1	89.0	88.8
C_β–H	91.9	90.2	91.9	90.6	91.9	89.5

Table 4: Calculated Bond Dissociation Energies (kcal mol^{-1}) of C–C and C–H bonds and comparison to ab initio computed values by da Silva and Bozzelli [54].

Table 5 reports the high-pressure limit rate parameters of initiation reactions in the non-Arrhenius form $A\,T^n \exp[-E_a/RT]$, where A is the frequency factor, E_a is the activation energy, and R is the gas constant. Units are: cm^3, mol, s, cal. Relative branching ratios at four different temperatures of 1000, 1500, 2000 and 2500 K are also shown. Whilst for propanal the decomposition is mainly initiated by C_α–C_β breaking throughout the temperature range explored, for $T < 1500$ K, the chain initiation for *n*-butanal and *n*-pentanal mainly occurs via the breakage of the C_β–C_γ bond to form the $\dot{C}H_2CHO$ radical. As already mentioned, the C_α–H bond cleavage contributes to the chain initiation only at high temperatures, and even then, it is still negligible due to its high activation energy.

Reactions	k_i [s^{-1}]	Branching Ratios [%]

	A_i	n_i	E_{ai}	1000 K	1500 K	2000 K	2500 K
propanal							
$C_2H_5CHO\leftrightarrow\dot{C}H_3+\dot{C}H_2CHO$	1.16E+25	–2.80	85718.	32.9	31.4	29.7	27.1
$C_2H_5CHO\leftrightarrow\dot{C}_2H_5+H\dot{C}O$	1.34E+26	–3.00	86406.	66.5	65.6	62.1	56.0
$C_2H_5CHO\leftrightarrow C_2H_5\dot{C}O+\dot{H}$	9.42E+16	–0.43	89167.	0.6	2.7	6.6	12.2
$C_2H_5CHO\leftrightarrow\dot{C}_2H_4CHO\text{-}1+\dot{H}$	1.22E+15	–0.08	91694.	0.0	0.2	0.7	1.5
$C_2H_5CHO\leftrightarrow\dot{C}_2H_4CHO\text{-}2+\dot{H}$	5.80E+17	–0.52	101476.	0.0	0.1	0.9	3.2
n-butanal							
$n\text{-}C_3H_7CHO\leftrightarrow\dot{C}H_3+\dot{C}_2H_4CHO\text{-}2$	1.09E+24	–2.25	90369.	4.1	14.4	26.2	36.2
$n\text{-}C_3H_7CHO\leftrightarrow\dot{C}_2H_5+\dot{C}H_2CHO$	5.04E+27	–3.50	84479.	67.3	52.3	40.5	31.5
$n\text{-}C_3H_7CHO\leftrightarrow n\dot{C}_3H_7+H\dot{C}O$	7.49E+27	–3.51	86758.	28.4	32.1	30.0	26.1
$n\text{-}C_3H_7CHO\leftrightarrow n\text{-}C_3H_7\dot{C}O+\dot{H}$	2.72E+17	–0.58	88995.	0.2	1.1	3.0	5.5
$n\text{-}C_3H_7CHO\leftrightarrow\dot{C}_3H_6CHO\text{-}1+\dot{H}$	3.62E+15	–0.23	91529.	0.0	0.1	0.3	0.7
n-pentanal							
$n\text{-}C_4H_9CHO\leftrightarrow\dot{C}H_3+\dot{C}_3H_6CHO\text{-}3$	1.18E+22	–1.61	90120.	3.3	9.9	16.5	22.0
$n\text{-}C_4H_9CHO\leftrightarrow\dot{C}_2H_5+\dot{C}_2H_4CHO\text{-}2$	2.84E+24	–2.24	89004.	17.1	33.4	42.1	45.8
$n\text{-}C_4H_9CHO\leftrightarrow n\dot{C}_3H_7+\dot{C}H_2CHO$	1.70E+27	–3.31	84704.	57.9	35.6	23.1	16.0
$n\text{-}C_4H_9CHO\leftrightarrow n\dot{C}_4H_9+H\dot{C}O$	1.20E+26	–2.94	86380.	21.6	20.4	16.8	13.7
$n\text{-}C_4H_9CHO\leftrightarrow n\text{-}C_4H_9\dot{C}O+\dot{H}$	1.64E+17	–0.50	89262.	0.1	0.6	1.3	2.1
$n\text{-}C_4H_9CHO\leftrightarrow\dot{C}_4H_8CHO\text{-}1+\dot{H}$	4.06E+14	0.11	91691.	0.0	0.1	0.2	0.4

Table 5: High-pressure limit rate parameters of initiation reactions and relative branching ratios at different temperatures [units are: cm^3, mol, s, cal].

3.2.2 H-abstraction reactions

Rate constant for abstractions of the acyl H-atom at the α position were estimated by analogy with the same site in formaldehyde and acetaldehyde. The presence of the H–C=O groups leads to the formation of resonantly stabilized radicals and the reactivity of the H-atoms in the β site is slightly enhanced with respect to secondary H-atoms in alkanes. This fact is also evident observing the enthalpy of formation in Table 3 and it is further supported by the kinetic study of 3-pentanone oxidation by Serinyel *et al.* [73]. Rate constants for abstractions from the remaining secondary and primary H-atoms were adopted according to their values used for *n*-alkanes [77].

Rate constants for this class of reactions need to be defined for all the H-atom abstracting radicals.

To maintain an internal consistency inside NUIG and POLIMI mechanisms, rate parameters for H-atom abstraction reactions are defined in two different ways, as will be discussed below.

3.2.3 Radical Decomposition Reactions

Arrhenius parameters for the decomposition of α-radicals to form CO were taken from the evaluation by Simmie [74] for 1-oxo-butyl radical ($n\text{-}C_3H_7\dot{C}O$) decomposition to *n*-propyl radical and CO. β-scission to form ketene and C_{n-2} alkyl radical has also been included in the kinetic scheme, based on the following rationale. Methyl radical addition to ketene to form 1-oxo-propyl radical ($C_2H_5\dot{C}O$) was taken as a reference and the kinetic parameters were estimated by analogy with methyl radical addition to propylene [75]. Rate constants for the analogous β-scission of 1-oxo-butyl and 1-oxo-pentyl radical (*n*-$C_4H_9\dot{C}O$) were based on the *ab initio* calculations of Huynh and Violi [76].

For the β-radical decomposition to form acrolein (C_2H_3CHO, 1-propenal) and an alkyl radical the recommended values of Curran [75] for the reverse addition reaction are used. Rate parameters for the dehydrogenation reactions of $\dot{C}_2H_4CHO$-1 radical to form acrolein or methylketene are derived from the kinetic values of the reverse $\dot{H}$-atom addition to propylene to give *iso*-propyl radical. Methyl and ethyl radical addition to propylene to form the secondary radicals were used to derive the corresponding decomposition of β-radicals of *n*-butanal and *n*-pentanal, forming acrolein and a methyl or an ethyl radical, respectively.

β-scission of γ-radicals to produce formyl radicals and alkenes, were based on computations of *n*-butanal radical decomposition by Huynh and Violi [76]. The symmetry effect was accounted for in the $H\dot{C}O$ addition on ethylene. The γ-radical of pentanal ($\dot{C}_4H_8CHO$-2) can also form a methyl radical and 1-butenal. Methyl radical addition to acrolein was used as a reference reaction.

Again, the *n*-butanal calculations by Simmie [74] were adopted for the decomposition of δ-radicals to form ethylene (or propylene) and $\dot{C}H_2CHO$ radical.

Finally, the decomposition of the ε-radical ($\dot{C}_4H_8CHO$-4) of *n*-pentanal to produce ethylene and the γ-radical of propanal were based on analogy with the addition of alkyl radicals to ethylene, as suggested by Orme *et al.* [77].

Table 6 summarizes the decomposition reactions and relating kinetic parameters, together with literature references.

3.2.4 Radical Isomerization Reactions

Radical isomerization reactions, i.e. internal H-atom shift through 3-, 4-, 5- and 6- membered ring intermediates, were also considered. Reaction rate constants were estimated according general rules [78–80]. The activation energy was estimated through Evans-Polanyi correlations accounting for reaction enthalpy of the H-atom shift reaction and the ring strain energy associated with ring formation in the transition state. Frequency factors were estimated on the basis of hindered rotor effects. As the ring intermediate gets bigger, the reactions become energetically more favored due to lower ring strain energies, but conversely are entropically inhibited due to the loss of internal rotors.

Isomerization reactions of the different radicals and kinetic parameters are reported in Table 6.

Reaction				
propanal radicals	*A*	*n*	*Ea*	*[ref]*
$\dot{C}_2H_4CHO$-2 <=> $C_2H_5\dot{C}O$	3.80E+10	0.67	30200.0	*[78]*
$\dot{C}_2H_4CHO$-1 <=> $C_2H_5\dot{C}O$	3.56E+10	0.88	37300.0	"
$C_2H_5\dot{C}O$ <=> CO + $\dot{C}_2H_5$	5.78E+14	0.00	16843.5	**[74]*
$\dot{C}H_3$ + CH_2CO <=> $C_2H_5\dot{C}O$	1.76E+04	2.48	6130.0	**[75]*

$\dot{H}$ + C_2H_3CHO <=> $\dot{C}_2H_4CHO$-1	4.24E+11	0.51	1230.0	*[75]
$\dot{H}$ + CH_3CHCO <=> $\dot{C}_2H_4CHO$-1	4.24E+11	0.51	1230.0	*[75]
$H\dot{C}O$ + C_2H_4 <=> $\dot{C}_2H_4CHO$-2	2.56E+02	2.89	6728.4	*[76]
n-butanal radicals				
$\dot{C}_3H_6CHO$-3 <=> n$C_3H_7\dot{C}O$	7.73E+11	0.00	15464.4	[78]
$\dot{C}_3H_6CHO$-2 <=> n$C_3H_7\dot{C}O$	3.80E+10	0.67	32100.0	″
$\dot{C}_3H_6CHO$-1 <=> n$C_3H_7\dot{C}O$	3.56E+10	0.88	37300.0	″
n$C_3H_7\dot{C}O$ <=> n$\dot{C}_3H_7$+CO	5.78E+14	0.00	16843.5	[74]
$\dot{C}_2H_5$ + CH_2CO <=> n$C_3H_7\dot{C}O$	3.33E+02	2.73	13953.9	[76]
$\dot{C}H_3$ + C_2H_3CHO <=> $\dot{C}_3H_6CHO$-1	1.76E+04	2.48	6130.0	*[75]
$H\dot{C}O$ + C_3H_6 <=> $\dot{C}_3H_6CHO$-2	1.28E+02	2.89	6728.4	[76]
$\dot{C}_3H_6CHO$-3 <=> $\dot{C}H_2CHO$ + C_2H_4	3.95E+13	0.00	22316.3	[74]
n-pentanal radicals				
$\dot{C}_4H_8CHO$-4 <=> n$C_4H_9\dot{C}O$	3.67E+12	–0.60	7090.0	[78]
$\dot{C}_4H_8CHO$-3 <=> n$C_4H_9\dot{C}O$	7.85E+11	–0.12	16800.0	″
$\dot{C}_4H_8CHO$-2 <=> n$C_4H_9\dot{C}O$	3.80E+10	0.67	32100.0	″
$\dot{C}_4H_8CHO$-1 <=> n$C_4H_9\dot{C}O$	3.56E+10	0.88	37300.0	″
n$C_4H_9\dot{C}O$ <=> p$\dot{C}_4H_9$ + CO	5.78E+14	0.00	16843.5	*[74]
n$\dot{C}_3H_7$ + ch2co <=> n$C_4H_9\dot{C}O$	3.33E+02	2.73	13953.9	*[76]
$\dot{C}_2H_5$ + C_2H_3CHO <=> $\dot{C}_4H_8CHO$-1	8.80E+03	2.48	6130.0	*[75]
$H\dot{C}O$ + C_4H_8-1 <=> $\dot{C}_4H_8CHO$-2	1.28E+02	2.89	6728.4	[76]
$\dot{C}H_3$ + C_3H_5CHO <=> $\dot{C}_4H_8CHO$-2	1.76E+04	2.48	6130.0	*[75]
$\dot{C}H_2CHO$ + C_3H_6 <=> $\dot{C}_4H_8CHO$-3	1.88E+02	3.11	3660.0	*[74]
$\dot{C}_2H_4CHO$-2 + C_2H_4 <=> $\dot{C}_4H_8CHO$-4	1.32E+04	2.48	6130.0	*[77]

Table 6: Rate parameters of decomposition and isomerization reactions of aldehyde radicals [units are: cm^3, mol, s, cal] and references (* extended analogy as discussed in this paper).

Due to their possible competing effect, a comparison of decomposition and isomerization rate constants of each radical is relevant. Figure 8 shows this comparison for *n*-pentanal radicals in the temperature range 1000–2500 K. The 1-5 isomerization reaction of the ε-radical in Figure 8d prevails over the decomposition channel at temperatures lower than ~1430 K. The remaining figures show that generally, the decomposition paths dominate. Moreover, Figure 8b shows that for *n*-pentanal γ-radical ($\dot{C}_4H_8CHO$-2) the decomposition reaction to form 3-butenal and a methyl radical prevails over the alternate channel generating 1-butene and a formyl radical. Decomposition of the α-radical (1-oxo-pentyl radical, *n*-$C_4H_9\dot{C}O$) to form CO and an *n*-butyl radical largely prevails over the 1-5 isomerization reaction in the complete range of temperature. For this reason reaction rate constants for the α-radical are not reported in Figure 8. A similar analysis for propanal and *n*-butanal is reported in the Supplementary Material.

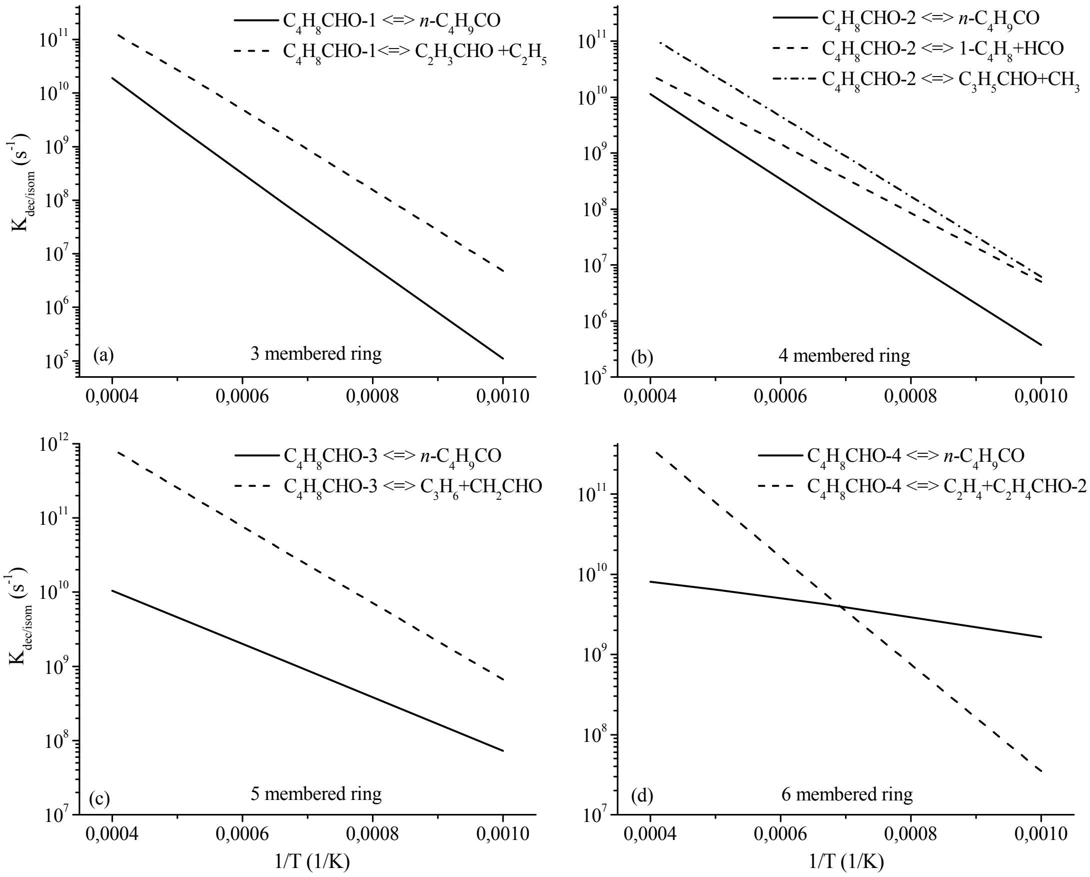

Figure 8: Isomerization (solid lines) and decomposition (dashed lines) reactions of n-pentanal ε-radical (a), δ-radical (b), γ-radical (c), β-radical (d).

4. Numerical Methods and Overall Kinetic Mechanisms

All numerical simulations were performed using either the OpenSMOKE code, which is an upgraded and extended version of the well-tested DSMOKE code. A shock tube is considered a constant volume batch system. The conservation equations with proper boundary conditions were discretized by means of conventional finite differencing techniques with non-uniform mesh spacing for the simulation of premixed laminar flames. A mixture-averaged formula was also used to compute multicomponent diffusion coefficients. Further details of the numerical methods are reported elsewhere [81–83].

The computed sensitivity coefficient, S_y, is normalized (s_y) as follows:

$$s_y = \frac{\delta \ln y}{\delta \ln A} = \frac{A}{y}\frac{\delta y}{\delta A} = \frac{A}{y} S_y$$

where y is the species concentration or the ignition delay time and A the generic frequency factor.

The Transport Data Estimator package of the Reaction Mechanism Generator software of Green and co-workers has been used to provide relevant transport properties [84].

4.1 NUIG Kinetic Mechanism

The aldehyde mechanism was coupled with the NUIG C_0–C_4 sub-mechanism, recently revised and validated as reported in several recent studies [55–60].

H-atom abstraction rates at the β secondary site forming $\dot{C}_4H_8CHO$-1 radicals were based on those for secondary H-atom abstractions in ketones. Rate constants for H-abstractions by $\dot{O}H$ and $H\dot{O}_2$ radicals were taken from the *ab initio* calculations for ethylmethyl ketone by Zhou *et al.* [85] and by Mendes *et al.* [86] respectively.

Before coupling the aldehyde sub-mechanism with the NUIG kinetic scheme, some modifications were made. The total initiation rate constant for *n*-butanal has been increased of a factor of 1.5 with respect to the calculated reaction rates previously discussed in Section 3.2.1. H-atom abstraction from the α carbonyl site has been decreased by about 20% with respect to the reference abstraction from acetaldehyde. Rate constants for abstraction reactions by $\dot{H}$, $\dot{O}H$ and $H\dot{O}_2$ radicals are listed in the Supplementary Material.

The overall kinetic model, with thermo and transport properties, consisting of 2,011 reactions and 329 species is available as part of the Supplementary Material.

4.2 POLIMI Kinetic Mechanism

Before coupling the aldehyde sub-mechanism with POLIMI kinetic scheme, some modifications have been applied.

While Troe fit parameters have been included for propanal to account for the pressure dependency of unimolecular reactions, *n*-butanal and *n*-pentanal initiations are described only by the high-pressure limit rate constants, due to the marginal effect of pressure dependency.

Metathesis reactions are treated according to the systematic approach described by Ranzi *et al.* [87]. The reactivity of primary and secondary H-atoms are considered to be the same as those for alkanes. Similar to the acyl H-atoms of formaldehyde and acetaldehyde, H-atom abstraction on the α site requires a correction of –4500 cal mol^{-1} to be applied to the activation energy for H-atom abstraction of a primary H-atom from a methyl group. With regards to abstraction from the β-site leading to resonantly stabilized radicals, a correction factor of about 1.3 has been applied to increase the frequency factor of the secondary H-atom abstraction. In order to improve the overall agreement with the complete experimental dataset, H-atom abstraction rates by $\dot{H}$ atoms and $H\dot{O}_2$ radicals have been increased, primarily at the α-site for all of the aldehydes. Rate constants for abstraction reactions by $\dot{H}$, $\dot{O}H$ and $H\dot{O}_2$ radicals are listed in the Supplementary Material.

Figure 6 shows that the lifetime of large radicals is so short at high temperatures that they decompose and isomerize without significant interactions with the remaining mixture. When parallel competing reactions are absent or not strongly dependent on temperature, larger radicals can be conveniently and directly substituted by their reaction products. Therefore, it is possible to assume them as being directly transformed into their products which are already part to the C_0–C_4 mechanism [88]. This is the advantage of a lumped approach: it leads to a reduction of the total number of species needed to describe the overall oxidation process. The analysis of Figure 6 highlights that only the ε-radical ($\dot{C}_4H_8CHO$-4) of pentanal shows a temperature dependent competition between isomerization and decomposition rates at high-temperatures. Therefore, it is convenient to keep the ε-radical inside the scheme. The four remaining radicals have been assumed to directly transform into their final products. The same assumption has been also applied to the intermediate radicals of *n*-butanal and propanal. The effect of these simplifications has proven to be of very limited importance in the high-temperature range of the analyzed conditions. At low-temperatures, interactions with oxygen forming peroxyl radicals will precede the decomposition of primary radicals; therefore, it would be necessary to increase the detail of the involved species.

The oxidation mechanism adopted here [61] consists of over 10,000 reactions and more than 350 species, and was developed based on hierarchical modularity. The thermochemical data for most species in the global mechanism were obtained from the CHEMKIN thermodynamic database [89, 90]. For those species whose thermodynamic data are not available in the literature, the group additivity method was used to estimate these properties [69].

The overall kinetic model, with thermo and transport properties, is available in CHEMKIN format from: http://creckmodeling.chem.polimi.it.

5. Model predictions and comparison with experimental data

The new experimental data on pyrolysis speciation and ignition delay times for the three aldehydes were used to validate the aldehyde sub-mechanism in both the kinetic models. Furthermore, propanal pyrolysis data by Lifshitz *et al.* [45] and ignition delay times by Akih-Kumgeh and Bergthorson [47] were also used. Similarly, *n*-butanal ignition delay times measured by Davidson *et al.* [50] and by Zhang *et al.* [52] were also compared with model predictions. Finally, comparisons with premixed laminar flame speeds of propanal and *n*-butanal by Veloo *et al.* [48, 49] complete this kinetic study. The current study, therefore considers all relevant experimental data which exist at present for long chain aldehydes, thus providing a comprehensive evaluation of mechanism performance. A summary of the experimental data at which the aldehydes mechanisms were validated in this study is reported in the Supplementary Material.

5.1 Pyrolysis in shock tubes

Propanal pyrolysis of a 1% fuel mixture in argon was studied in a single-pulse shock tube by Lifshitz *et al.* [45] over the temperature range 970–1300 K. Experimental data and modeling predictions are shown in Figure 9 for the NUIG and POLIMI mechanisms. Furthermore, Figure 10 compares experimental data from this work and predicted concentration profiles for propanal (3%) decomposition in argon. Propanal undergoes decomposition at ~1050 K according to both the experimental data sets and the mechanisms slightly under-predict fuel conversion: an overall good agreement is observed for the main products (CO and C_2H_4), as well as for the minor hydrocarbon species, particularly in terms of their relative concentrations. Analysis of the mechanisms shows that chain radical initiation occurs via unimolecular decomposition reactions involving a C–C bond cleavage, and propanal decomposition mainly occurs via H-atom abstraction reactions by $\dot{H}$ atoms and $\dot{C}H_3$ radicals.

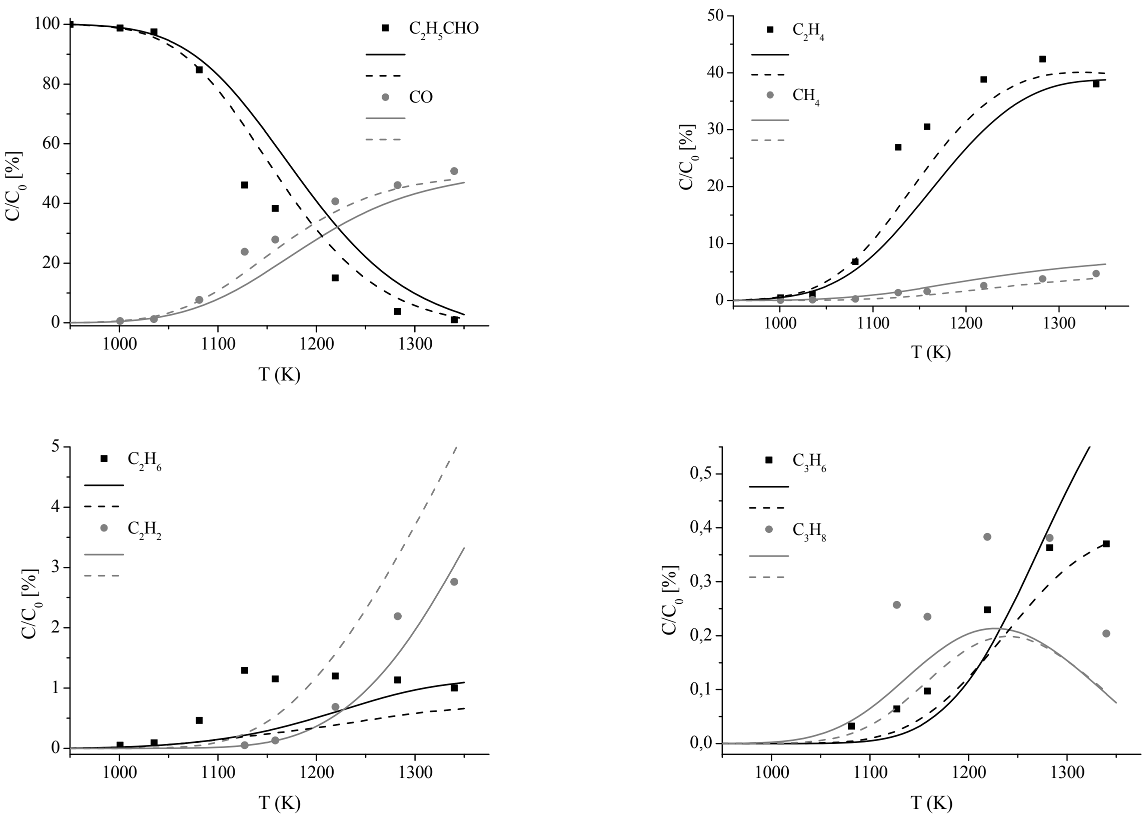

Figure 9: Predicted and experimental concentration profiles from shock tube pyrolysis of 1% propanal in argon [45]. Experimental (symbols), POLIMI mechanism (solid lines) and NUIG mechanism (dashed lines).

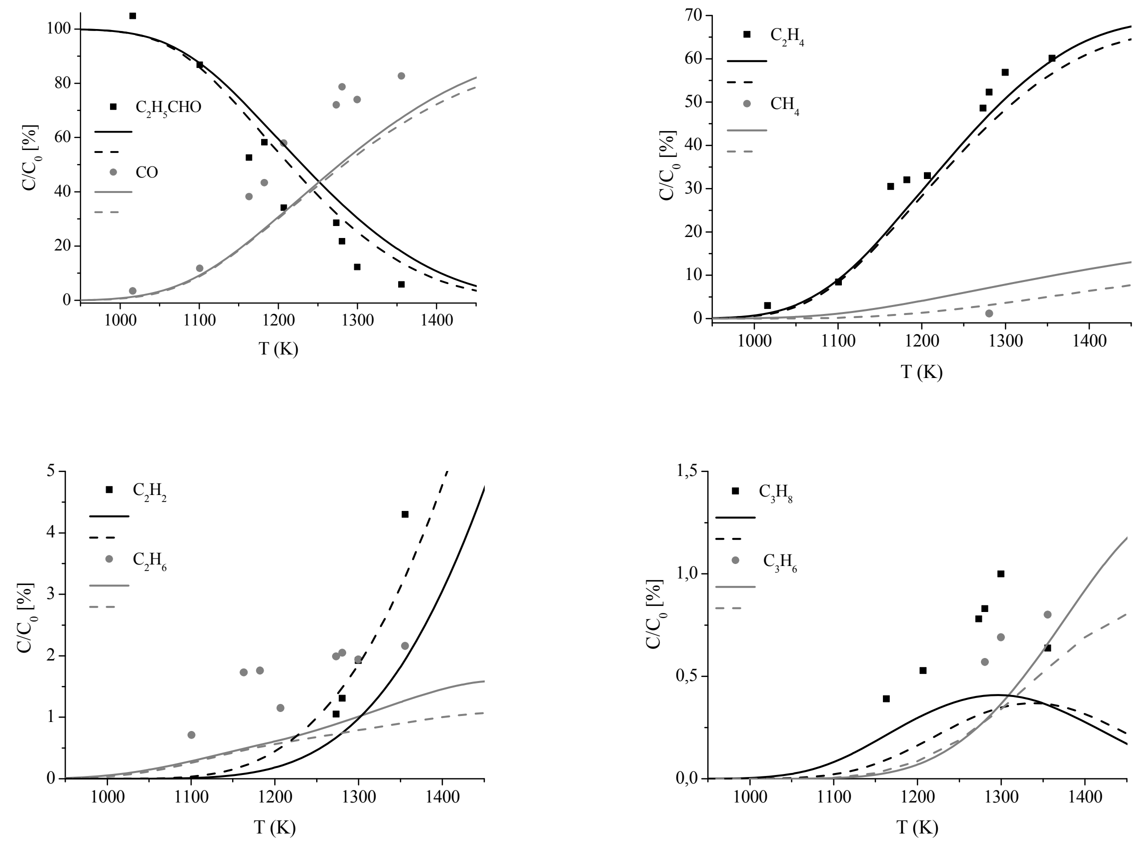

Figure 10: Predicted and experimental concentration profiles from shock tube pyrolysis of 3% *n*-butanal in argon. Experiments (symbols), POLIMI mechanism (solid lines) and NUIG mechanism (dashed lines).

The POLIMI mechanism under-predicts C_2H_2 formation reported in Figure 9 by ~40% at temperatures higher than 1200 K and even larger deviations are observed in Figure 10. The chemistry of the vinyl radical ($\dot{C}_2H_3$) is responsible for this under-prediction. H-atom abstractions from acrolein (C_2H_3CHO) are the main pathways generating acetylene, either through the vinyl radical formed by the CO elimination of the α radical, or via the β-scission of the γ radical to give formyl radical. The same chemistry is responsible for the over-prediction of acetylene observed for the NUIG mechanism in Figure 9, while good agreement is observed in Figure 10. The under-predictions of propane and propylene can be attributed to the slow rate of radical recombination reactions, i.e. a relatively low importance of the chain initiation reactions. The results shown in Figure 9 and Figure 10 are considered to be well within the expected experimental uncertainties.

Figure 11 compares experimental and predicted concentration profiles for *n*-butanal (3%) decomposition in argon. Predictions of fuel conversion as well as the major products, such as CO and ethylene, are in very good agreement with the experimental observations. Smaller hydrocarbons detected in the measurements (CH_4, C_2H_2, C_2H_6, C_3H_6 and C_3H_8), are also very well captured by both models. The main relative deviations are observed in the trace amount of propane; this under-prediction is due to methyl and ethyl radical recombination.

Figure 12 shows a global rate of production analysis performed at 1200 K, for both the NUIG and POLIMI mechanisms. The chain initiation occurs *via* unimolecular decomposition reactions, the successive decomposition of formyl, ethyl and propyl radical intermediates leads to the generation of $\dot{H}$ atoms and $\dot{C}H_3$ radicals, which are responsible, via H-atom abstraction, for ~90% of fuel consumption, at 1200 K.

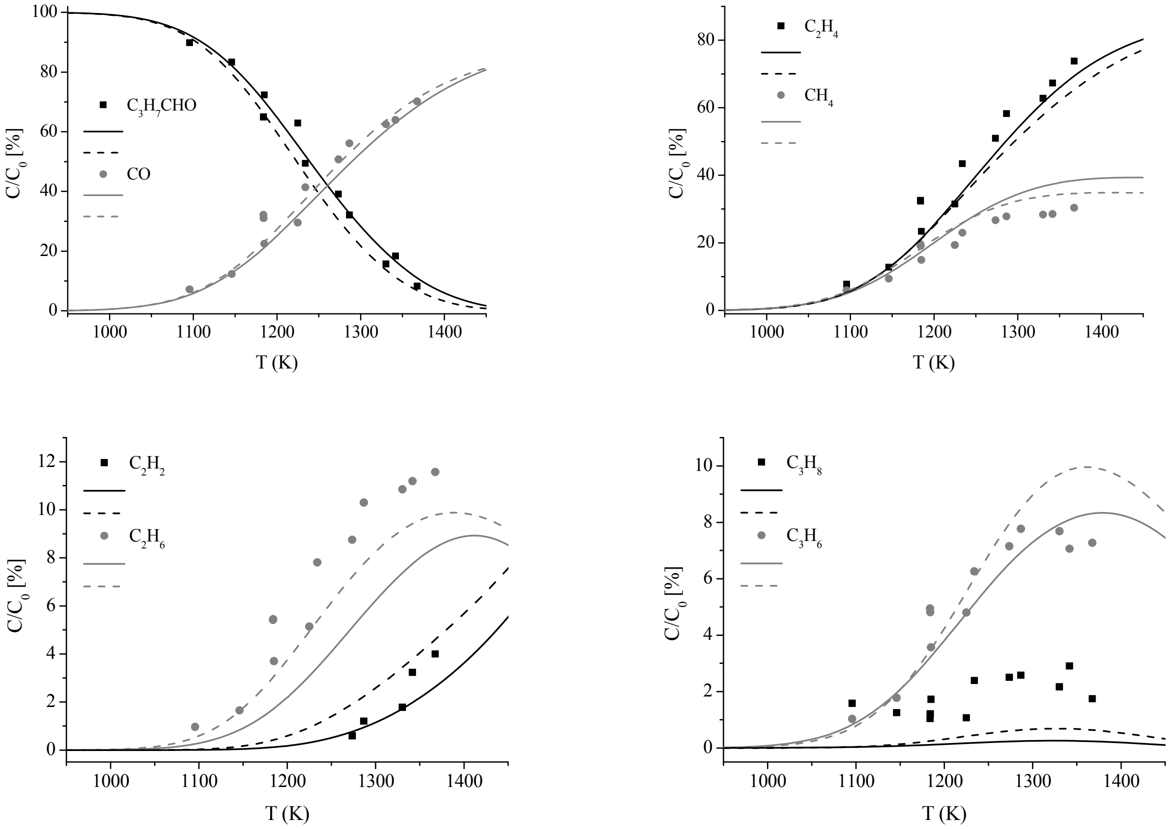

Figure 11: Predicted and experimental concentration profiles from shock tube pyrolysis of 3% *n*-butanal in argon. Experiments (symbols), POLIMI mechanism (solid lines) and NUIG mechanism (dashed lines).

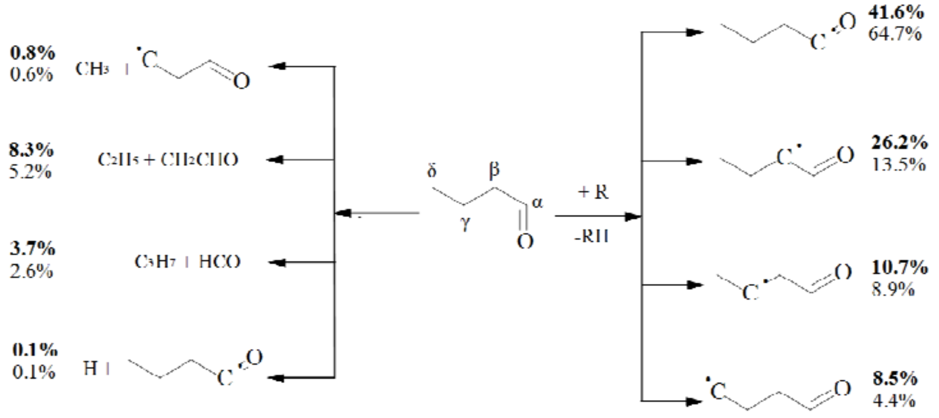
0.8%
0.6%
CH_3 +
8.3%
5.2%
$C_2H_5 + CH_2CHO$
3.7%
2.6%
C_3H_7 + HCO
0.1%
0.1%
H +
δ
β
γ
α
O
+ R
-RH
41.6%
64.7%
26.2%
13.5%
10.7%
8.9%
8.5%
4.4%

Figure 12: Global rate of production analysis carried out at 1200 K under the pyrolysis conditions studied as part of this work, NUIG mechanism (bold) and POLIMI mechanism (standard).

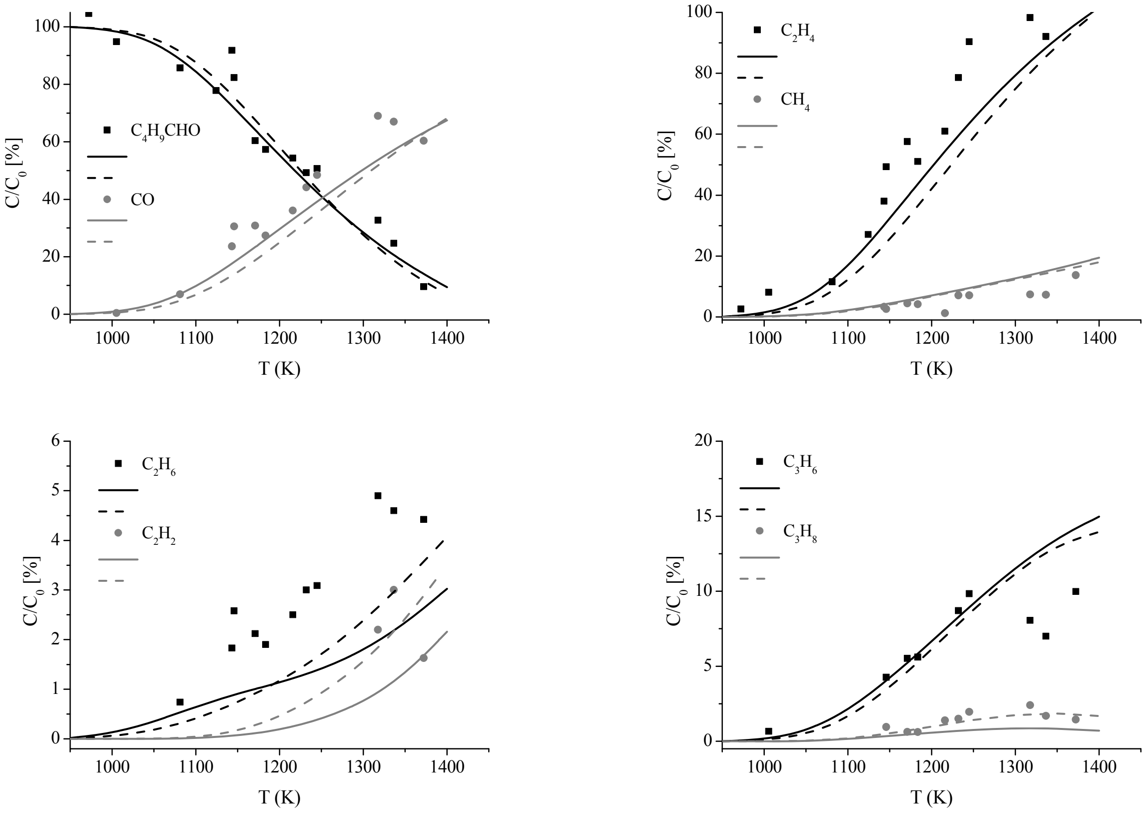

Figure 13: Predicted and experimental concentration profiles from shock tube pyrolysis of 3% *n*-pentanal in argon. Experiments (symbols), POLIMI mechanism (solid lines) and NUIG mechanism (dashed lines).

Figure 13 compares the species predictions by both mechanisms to experimental data for 3% *n*-pentanal pyrolysis in argon. Both of the models are able to reproduce the fuel conversion, indicating that *n*-pentanal starts to decompose at temperatures of ~1000–1050 K. Both of the mechanisms reproduce the relative importance of all species. The POLIMI mechanism tends to be slightly more reactive, better reproducing the major product species CO and ethylene. Within the experimental uncertainty, the two kinetic schemes satisfactorily reproduce the minor hydrocarbon species.

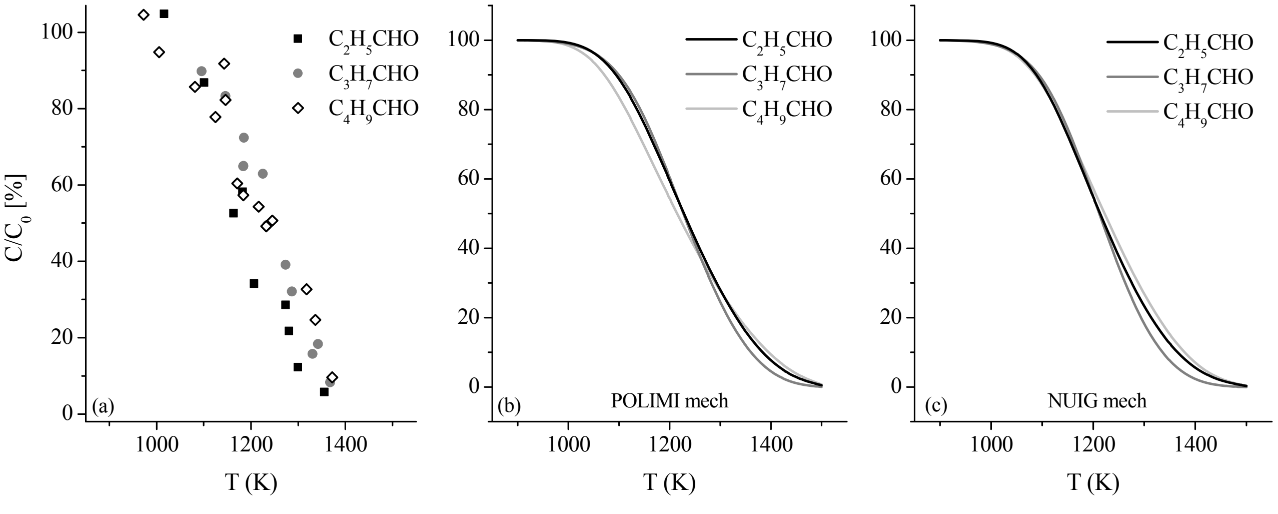

Figure 14: Fuel concentration profiles from shock tube pyrolysis (3% in argon), experiments from this work (a), POLIMI mechanism (b) and NUIG mechanism (c) predictions.

Figure 14 compares the relative reactivity of the three aldehydes. Experimentally the three aldehydes seem to behave very similarly for temperatures up to ~1200 K. Propanal shows the highest conversion rate for $T > 1200$ K, while no big differences are highlighted between *n*-pentanal and *n*-butanal. As schematically shown in Figure 5, this can be justified by the fact that H-atom abstractions from the highly reactive α and β positions of propanal result in a very high production of $\dot{\mathrm{H}}$ atoms, via β-scission reactions. Both of the mechanisms predict very similar reactivity up to ~1200 K, with butanal showing the highest conversion rate at higher temperatures.

3.1 Ignition delay times in shock tubes

3.1.1 Propanal

Ignition delay times measurements at 1 and 3 atm reflected pressures made in this study are shown in Figure 15 together with modeling predictions. Experiments were carried out using 1% fuel in O_2/argon as described in Table 2 (Section 2.2). While the mechanisms are in good or reasonable agreement with the experimental data at 3 atm under all investigated conditions, larger deviation are observed at atmospheric pressure. In this case, both of the mechanisms predict higher apparent activation energies, particularly at stoichiometric and fuel-lean conditions.

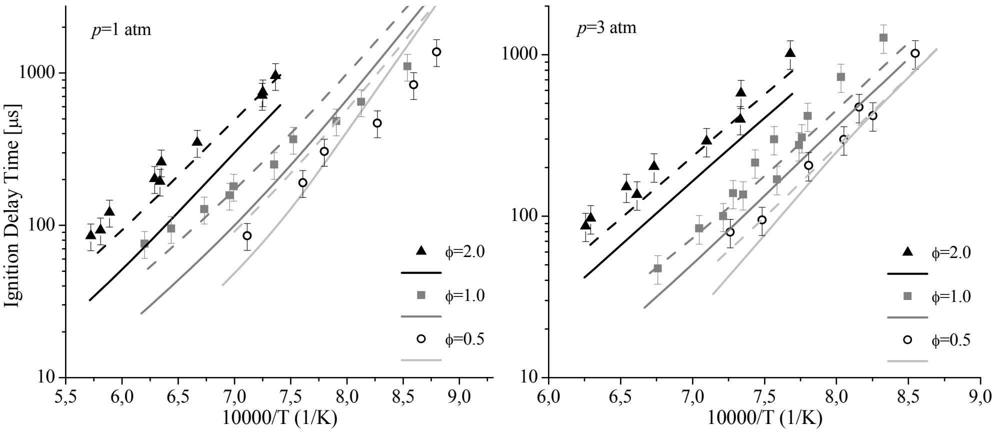

Figure 15: Predicted and experimental ignition delay times of 1 % propanal in O_2/Ar mixtures. Experiments (symbols), POLIMI mechanism (solid lines) and NUIG mechanism (dashed lines).

Figure 16 compares model predictions and ignition delay times measured by Akih-Kumgeh and Bergthorson [47]. In line with the previous observations of Figure 15, while good agreement is obtained at 12 atm pressure, at atmospheric pressure the activation energy is over-predicted by both mechanisms. The NUIG mechanism shows better agreement with the data of Akih-Kumgeh, primarily for stoichiometric conditions.

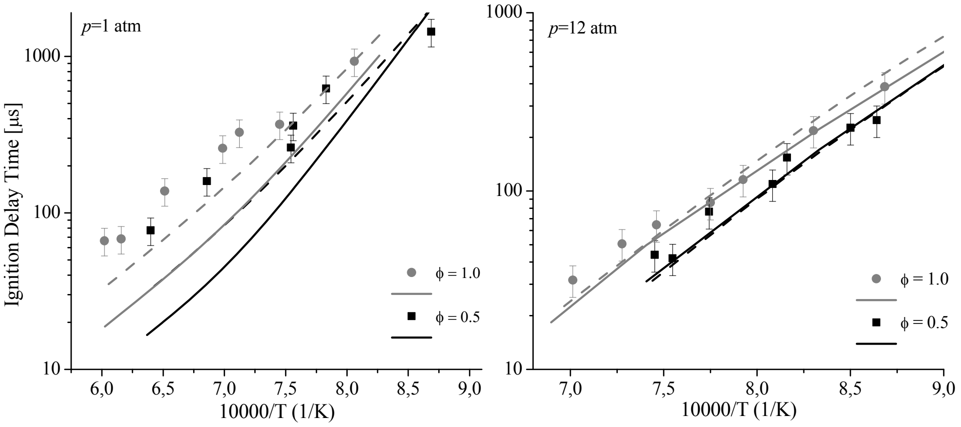

Figure 16: Predicted and experimental ignition delay times of O_2/Ar mixtures containing 1.25% propanal [47]. Experiments (symbols), POLIMI mechanism (solid lines) and NUIG mechanism (dashed lines).

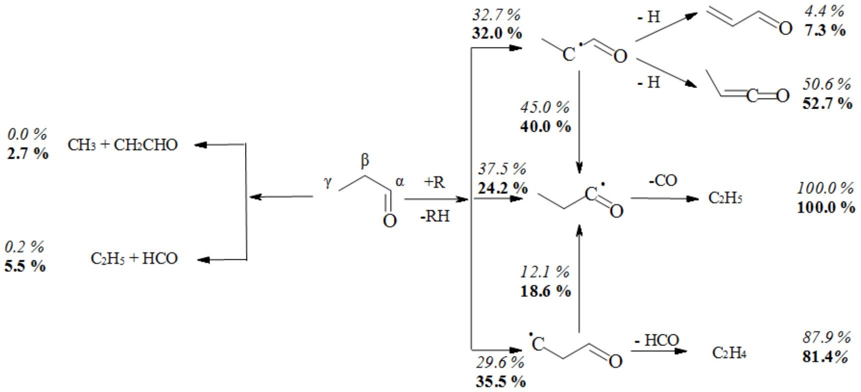

Figure 17: Rate of production analysis for 1% propanal in O_2/Ar mixtures at φ = 1.0, p = 1 atm. NUIG mechanism, T = 1150 K (italic) and 1620 K (bold).

Figure 17 shows a rate of production analysis at stoichiometric conditions, atmospheric pressure, and at temperatures of 1150 K and 1620 K for the NUIG mechanism. At 1620 K, the unimolecular decomposition pathways contribute ~8% to fuel consumption, being negligible at 1150 K. The fuel decomposition mostly occurs through the α channel, either via direct H-atom abstractions or due to isomerization of β and γ radicals, with a relevant formation of $\dot{C}_2H_5$ radicals. At 1620 K ethyl radicals mostly decompose to ethylene and $\dot{H}$ atoms promoting reactivity, while at 1150 K ethyl radicals can also react with molecular oxygen producing $H\dot{O}_2$ radicals, thus inhibiting the system.

Figure 18 shows the sensitivity coefficients of ignition delay times to rate constants in the NUIG mechanism. Sensitivity coefficients were calculated for each reaction via a brute force method, where a negative coefficient indicates a reaction promoting reactivity, i.e. decreases ignition delay times. Increasing the rates of H-atom abstraction reactions by $\dot{H}$ atoms decreases reactivity making ignition delay times longer. This is because by reacting with any species but O_2 a $\dot{H}$ atom is

removed from the system to form H_2, rather than reacting with O_2 to generate $\ddot{O}$ atoms and $\dot{O}H$

radicals which is the predominant chain-branching process for high temperature combustion. H-atom abstraction by $H\dot{O}_2$ radicals on the α site appears as a sensitive parameter at 1150 K, due to the subsequent decomposition of H_2O_2 to generate two $\dot{O}H$ radicals, which is highlighted as a promoting reaction. The importance of radical species such as formyl, methyl, vinyl and ethyl radicals is also highlighted, confirming the influence of reactions involving β-scission products such as ethylene and acrolein in the correct determination of propanal ignition.

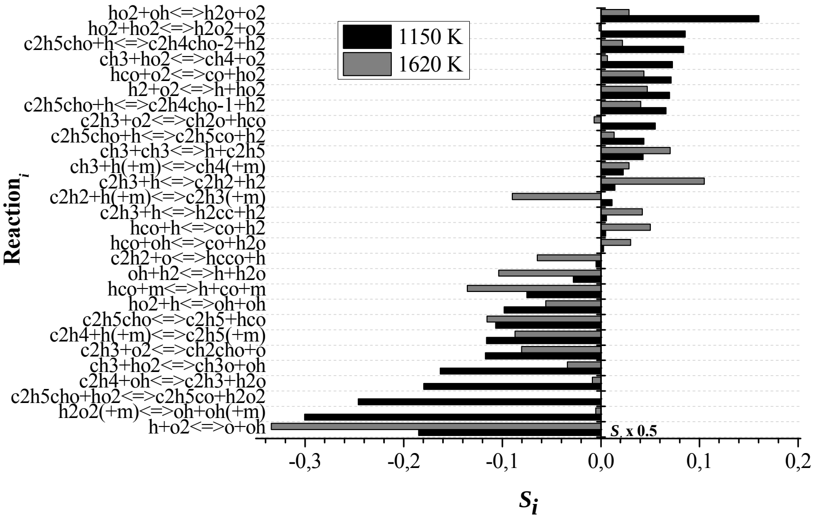

Figure 18: Sensitivity coefficients of ignition delay times to rate constants for 1% propanal in O_2/Ar mixtures at φ = 1.0, p = 1 atm, 1150 K (black bars) and 1620 K (grey bars). NUIG mechanism.

3.1.2 *n*-butanal

Figure 19 shows a comparison between experimental and calculated ignition delay times for mixture of 1% *n*-butanal in O_2/argon. Both of the mechanisms agree with the experimental data at the conditions tested, with the NUIG mechanism being consistently slower compared to the POLIMI mechanism. The larger deviations from the experimental observations, mainly in terms of apparent activation energies, can be observed for the POLIMI and NUIG mechanisms at 1 atm and φ = 0.5.

Figure 20 compares the mechanisms predictions with the experimental measurements of Davidson *et al.* [50], at two different dilutions. The NUIG mechanism reproduces the apparent activation energy in both cases, while the POLIMI mechanism being slightly faster, and thus over-predicts the activation energies, but is still in reasonable agreement with experiments.

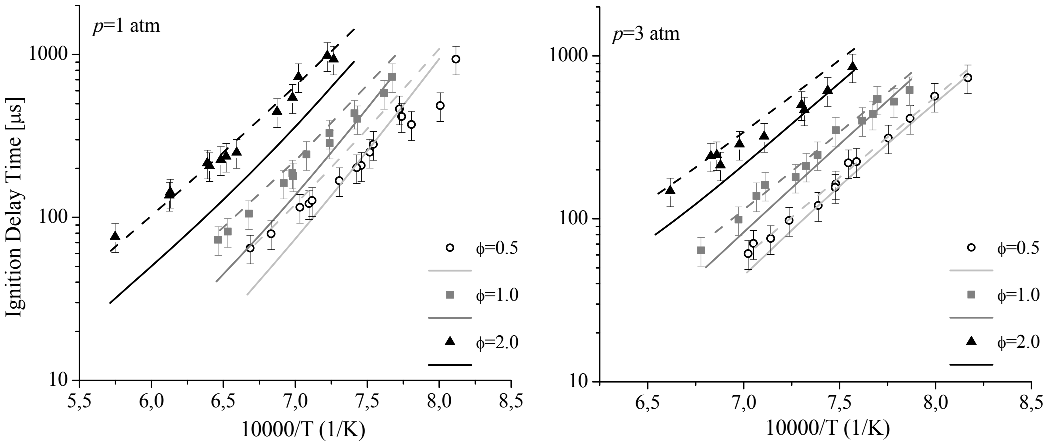

Figure 19: Predicted and experimental ignition delay times of O_2/Ar mixtures containing 1% *n*-butanal. Experiments (symbols), POLIMI mechanism (solid lines) and NUIG mechanism (dashed lines).

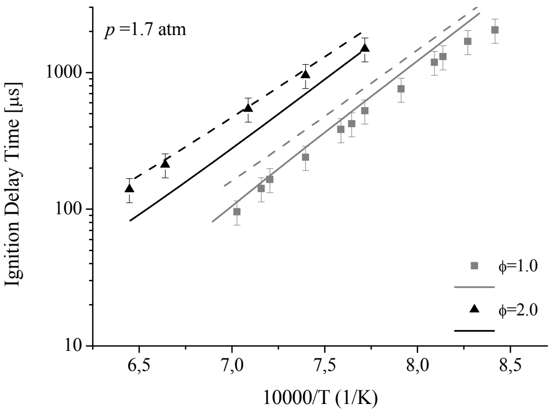

Figure 20: Predicted and experimental ignition delay times of O_2/Ar mixtures containing 1% *n*-butanal [50]. Experiments (symbols), POLIMI mechanism (solid lines) and NUIG mechanism (dashed lines).

Figure 21 compares all three sets of experimental data (our experiments at 1 atm, Zhang [52] at 1.3 atm and Davidson *et al.* [50] at 1.7 atm). Following the approach of Davidson *et al.* [50], all of the data have been scaled at 1.7 atm, assuming a scaling factor $p_{exp}/1.7^{-0.52}$. The experimental data agree under stoichiometric conditions, while the measurements of Zhang are notably faster under fuel-rich conditions. Figure 22 compares the experimental data from Zhang *et al.* [52] with model predictions. Both of the mechanisms tend to over-predict ignition delay times, particularly at 1.3 atm. The POLIMI mechanism reproduces these experiments more closely than the NUIG mechanism, which over-predicts the ignition delay times, particularly at atmospheric pressure. However, on the basis of the observations of Figure 21, the performances of the two mechanisms are considered to be in satisfactory agreement with the experimental data.

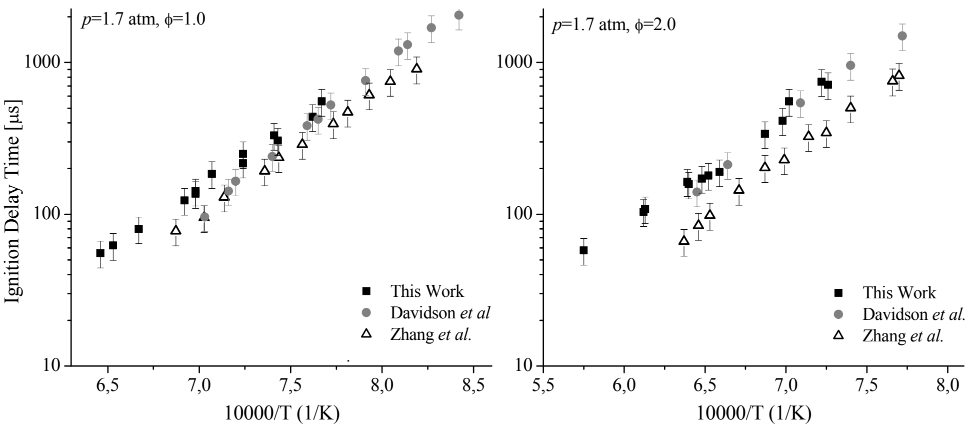

Figure 21: Comparison amongst experimental ignition delay times for *n*-butanal-O_2/Ar mixtures, scaled at 1.7 atm. This work: 1% fuel at 1 atm (squares); Zhang et al [52]: 1.2% fuel at 1.3 atm (triangles); Davidson *et al.* (circles) [50]: 1% fuel at 1.7 atm.

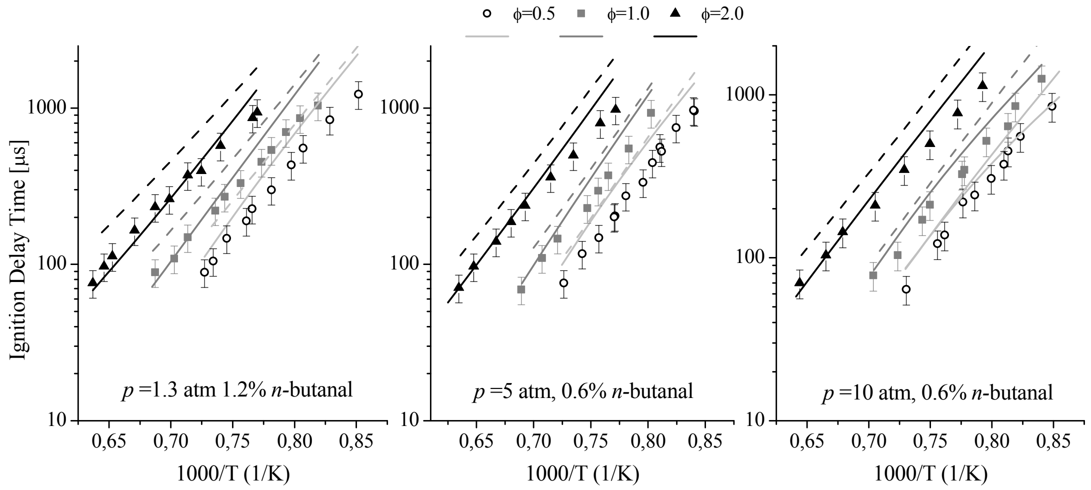

Figure 22: Predicted and experimental ignition delay times of *n*-butanal in O_2/Ar mixtures [52]. Experiments (symbols), POLIMI mechanism (solid lines) and NUIG mechanism (dashed lines).

Figure 23 shows a reaction path analysis carried out for fuel-lean (φ = 0.5) and fuel-rich (φ = 2.0) mixtures at 3 atm and 1320 K, with the NUIG mechanism. The unimolecular decomposition reactions accounts for 12.6% and 7.5% of fuel consumption under fuel-lean and fuel-rich conditions, respectively. H-atom abstraction from the α site is an important decomposition channel (~27.0 %). The β and γ sites show similar selectivities (20–30%), with β favored at fuel-rich conditions and γ at fuel-lean conditions. This can be explained on the basis of a higher production of $\dot{O}H$ radicals through the chain-branching reaction $\dot{H}+O_2\leftrightarrow\ddot{O}+\dot{O}H$, due to the higher concentration of oxygen in the system. $\dot{O}H$ radicals are then more likely to abstract on the γ site relative to the β site.

Figure 24 presents sensitivity coefficients of ignition delay times to rate constants at the same conditions shown in Figure 23, in order to identify the reactions controlling the auto-ignition behavior. Chain initiation reactions generating highly reactive radicals promote the system's reactivity at both conditions. Particularly, the breaking of the weak C_β–C_γ bond producing an ethyl radical and the breaking of the C_α–C_β bond producing a formyl radical exhibit some sensitivity.

Decreasing the oxygen concentration largely enhances the importance of small unsaturated species such as acetylene, ethylene, propylene and the parent radicals. H-atom abstraction by Ḣ atoms reduces the reactivity due to the competition with the branching reaction Ḣ+O_2↔Ö+ȮH. Furthermore, H-atom abstractions from the α site increase the ignition delay times due to the formation of 1-propyl radical, which decomposes to produce methyl radicals.

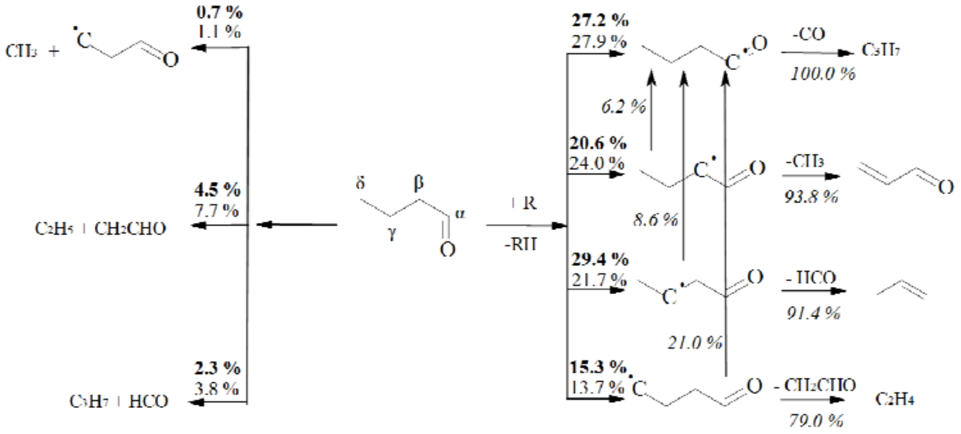

Figure 23: Rate of production analysis for 1 % *n*-butanal in O_2/Ar mixtures at *p*=3atm, *T*=1320 K at φ = 0.5 (bold) and φ = 2.0 (standard).

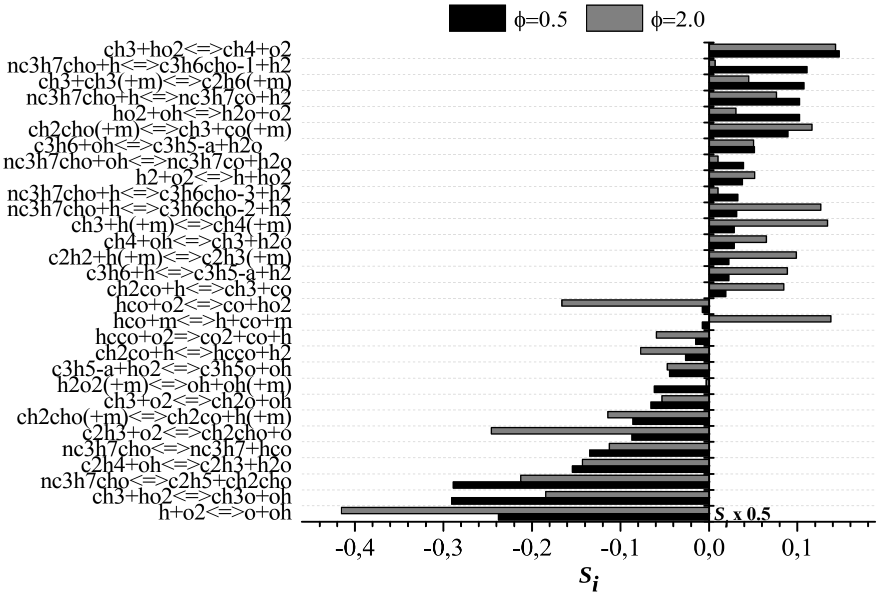

Figure 24: Sensitivity coefficients of ignition delay times to rate constants for 1 % *n*-butanal in O_2/Ar mixtures at *p* = 3 atm, *T* = 1320 K at φ = 0.5 (black bars) and φ =2.0 (grey bars).

3.1.3 *n*-pentanal

Experimental and calculated ignition delay times for 1% *n*-pentanal mixtures in O_2/Ar are reported in Figure 25 for conditions as described in Table 2. The NUIG mechanism captures the experimental data at every condition tested. The POLIMI mechanism tends to predict shorter ignition delay times for fuel-rich conditions particularly at atmospheric pressure. At 1850 K, the ignition delay time is under-predicted by a factor of three. Again, the model over-predicts the apparent activation energy. At 3 atm both of the models over-estimate the ignition delay time at fuel-lean conditions for temperatures below 1100 K. Low-temperature chemistry, outside the scope of this work, might have an effect at these conditions.

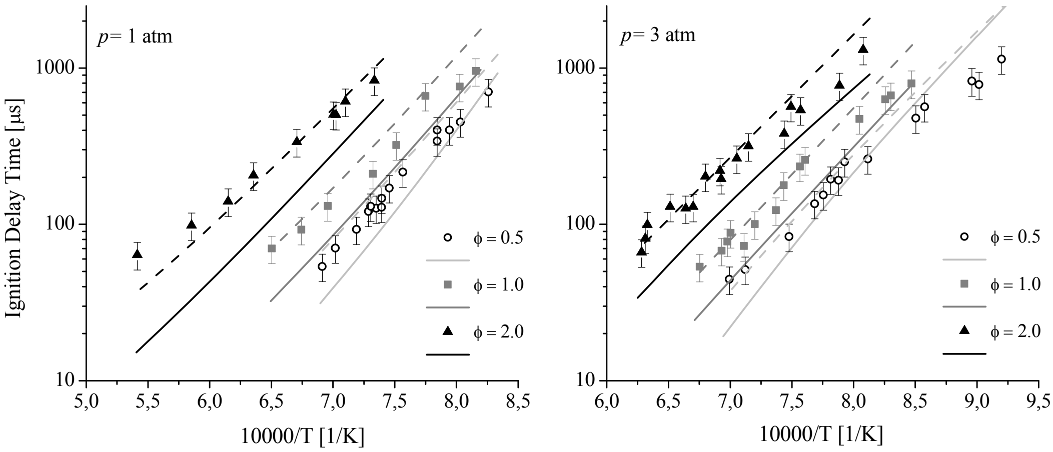

Figure 25: Predicted and experimental ignition delay times of O_2/Ar mixtures containing 1 % *n*-pentanal. Experiments (symbols), POLIMI mechanism (solid lines) and NUIG mechanism (dashed lines).

Figure 26 presents a rate of production analysis carried out for the POLIMI mechanism at intermediate conditions (φ =1.0, p = 2 atm, T = 1300 K). Unimolecular decomposition reactions account for less than 3.0% of *n*-pentanal consumption. Decomposition occurs mainly via H-atom abstraction from the α position (~54%), followed by abstraction from the γ and δ (~15%) positions. At the conditions investigated ~75% of the ε-radical ($\dot{C}_4H_8CHO$-4) isomerizes to the α-radical (*n*-$C_4H_9\dot{C}O$), which is assumed to eliminate CO (90%) and/or decompose to *n*-propyl and ketene (10%). As already discussed in Section 4.2, the POLIMI lumped mechanism only accounts for the ε-radical, the rate of production is simply obtained through a *de-lumping* procedure.

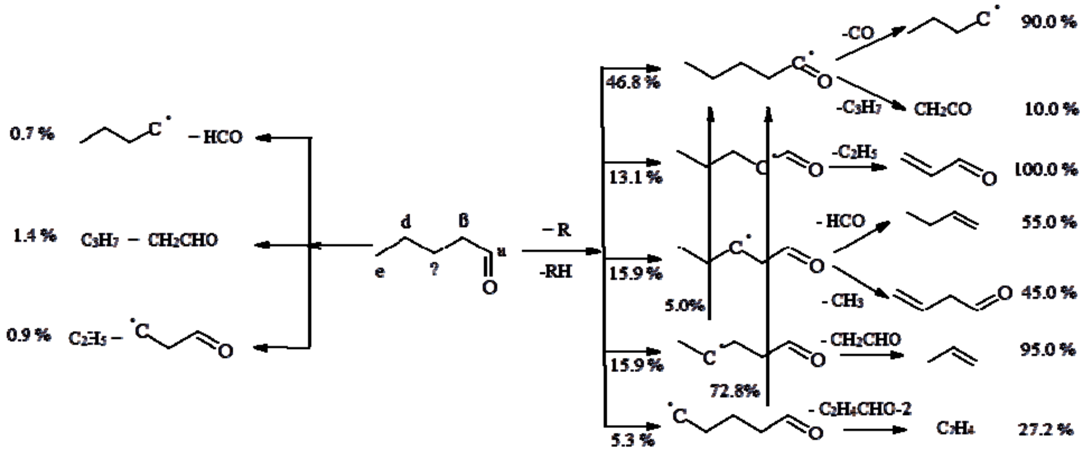

Figure 26: Rate of production analysis for 1 % *n*-pentanal in O_2/Ar mixtures at φ =1.0, p = 2 atm, T = 1300 K, POLIMI mechanism.

Figure 27 shows the sensitivity analyses of ignition delay times to rate constants for the NUIG and POLIMI mechanisms, at φ = 1.0, p = 2 atm, and T = 1300 K. With regards to fuel specific reactions, both of the mechanisms show that H-atom abstraction rates from the γ and δ positions have positive coefficients, i.e. they decrease reactivity (longer ignition delay times). Unimolecular initiation reactions enhance reactivity in the NUIG mechanism, whilst they are not highlighted as sensitive for the POLIMI mechanism. H-atom abstractions from the α position contribute to shorten ignition delay times for the POLIMI mechanism. Once again, the higher importance of the C_0–C_4 sub-mechanism is highlighted. To make the comparison more clear, the most sensitive branching reaction $\dot{H}+O_2\leftrightarrow\ddot{O}+\dot{O}H$, normalized to –1 for both the mechanisms, is not reported in Figure 27.

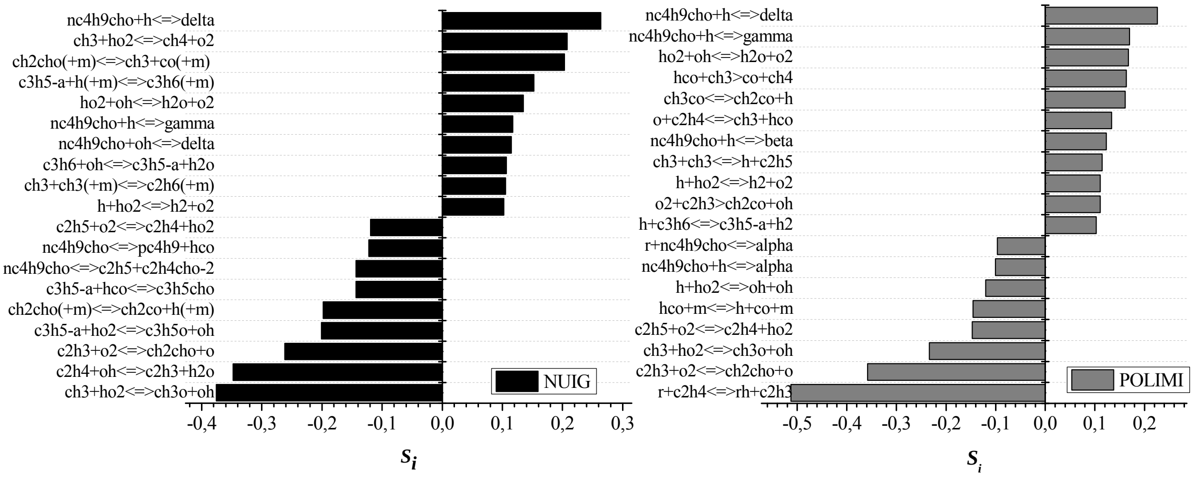

Figure 27: Sensitivity coefficients of ignition delay times to rate constants for 1 % n-pentanal in O_2/Ar mixtures at φ = 1.0, *p* = 2 atm, *T* = 1300 K. NUIG mechanism (black bars), POLIMI mechanism (grey bars).

3.2 Apparent activation energy of ignition delay times

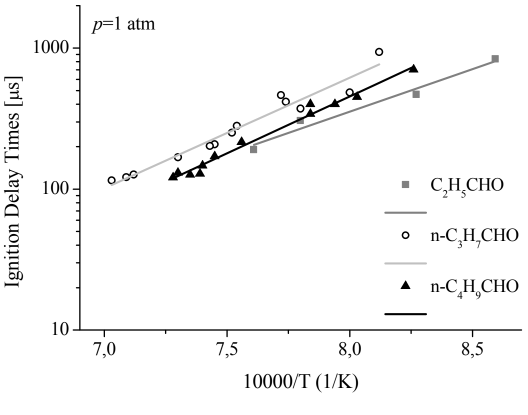

Figure 28: 1% fuel–O_2/Ar mixtures; φ = 0.5, *p* = 1 atm, experimental data from present work (symbols) and linear fit (lines).

Figure 28 compares the experimental ignition delay times at 1 atm and lean conditions for the three aldehydes. Propanal tends to be the faster to ignite, followed by *n*-pentanal and *n*-butanal. Based on oxygen concentration one would expect *n*-pentanal to be fastest followed by *n*-butanal and propanal. The reason for the observed trend, correctly reproduced by both of the mechanisms, is that there is a greater quantity of $\dot{H}$ atoms produced by primary propagation reactions during propanal oxidation. Conversely, methyl radicals are formed via the decomposition of β and γ radicals in *n*-butanal and *n*-pentanal, respectively. This figure also highlights the different apparent activation energies for propanal and *n*-pentanal.

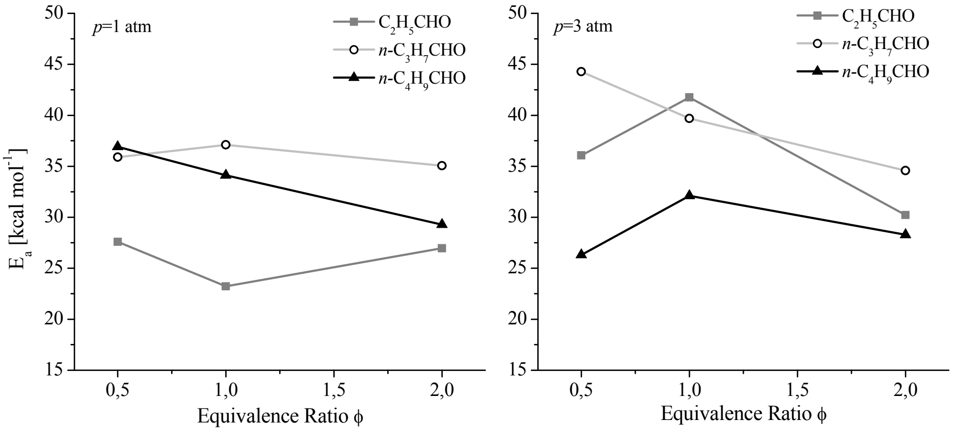

Figure 29: 1% fuel-O_2/Ar mixtures, experimental apparent activation energies E_a at 1 and 3 atm pressure.

Figure 29 shows a more detailed comparison of the apparent activation energies obtained in this work for the three aldehydes at 1 and 3 atm. Activation energies ranging from 23 to 45 kcal mol^{-1} are observed experimentally, without clear trends.

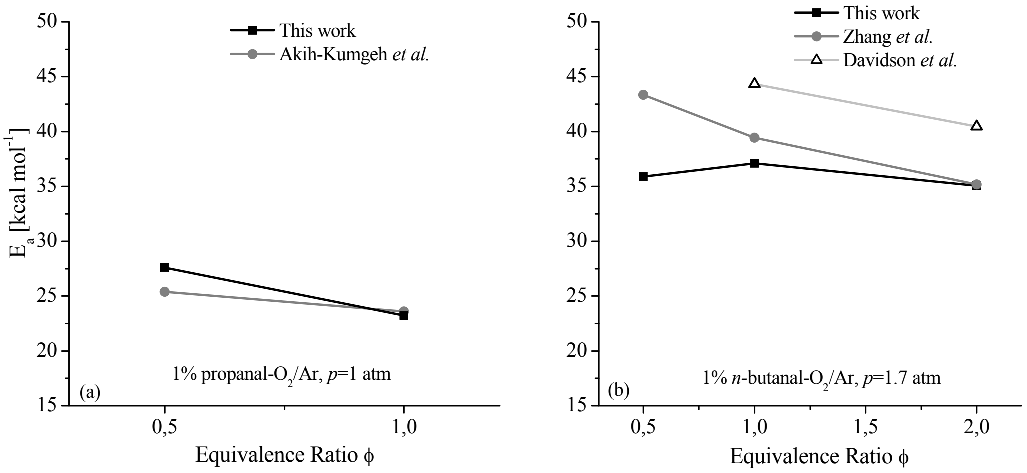

Figure 30: fuel-O_2/Ar mixtures, experimental apparent activation energies E_a.

To better understand this situation, Figure 30a shows a comparison of the apparent activation energy for propanal observed in this work with the data of Akih-Kumgeh and Bergthorson [47]. These data are very consistent and the differences are very small. Figure 30b presents a similar comparison for *n*-butanal. Here the activation energies are compared with the ones obtained from the data of Zhang et al. [52] and those of Davidson et al. [50]. All of these data show a decrease in activation energy going from stoichiometric to fuel-rich mixtures. Nevertheless, large deviations are still observed posing some questions on the reliability of the experimental data. As far as the predicted activation energies are concerned, the averages of previous simulations show that the NUIG mechanism over-estimates the activation energy of ~5 kcal mol^{-1}, while the POLIMI mechanism exceed by ~10 kcal mol^{-1}. The largest deviations are observed in both cases for fuel-lean conditions. A complete overview of experimental and calculated apparent activation energies is reported in the Supplementary Material.

3.3 Laminar flame speeds

3.3.1 Propanal

Figure 31 shows a comparison of experimental [48] and predicted laminar flame speeds for propanal/air mixtures at atmospheric pressure. Experimental and predicted peaks (53 vs 55.5 cm s^{-1}) are correctly placed at φ = 1.1–1.15. Both mechanisms over-predict the laminar flame speed at stoichiometric and fuel-rich conditions by 2–4 cm s^{-1}. Accounting for the experimental uncertainty represented in Figure 30 by the error bars (3.5–12.5%), the overall agreement of the mechanisms seems satisfactory.

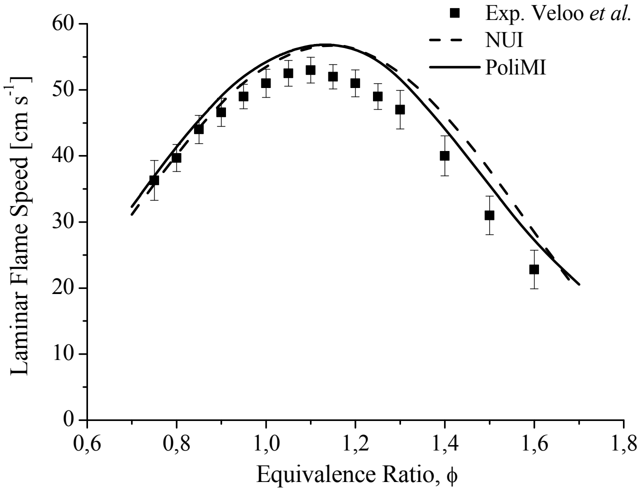

Figure 31: Experimental and computed laminar flame speeds of propanal/air flames at T_u = 343 K and p = 1 atm. Experimental data (symbols) by Veloo et al.[48], POLIMI mechanism (solid lines) and NUIG mechanism (dashed lines).

Figure 32 reports the sensitivity coefficients of laminar flame speed to rate constants for propanal/air flames at φ = 1.3, T_u = 343 K, using both mechanisms. H-atom abstraction reaction from the α site are sensitive in reducing the flame speed for both mechanisms. H-atom abstraction from the γ site has a positive sensitivity coefficient (flame propagation enhancer) in the NUIG mechanism. This is due to the fact that, while the γ radical forms $\dot{H}$ and CO from $H\dot{C}O$, ethyl radical can also react with a $\dot{H}$ atom forming two methyl radicals. Results confirm that the chemistry of propanal at flame temperatures is dominated by the C_0–C_4 portion of the mechanisms.

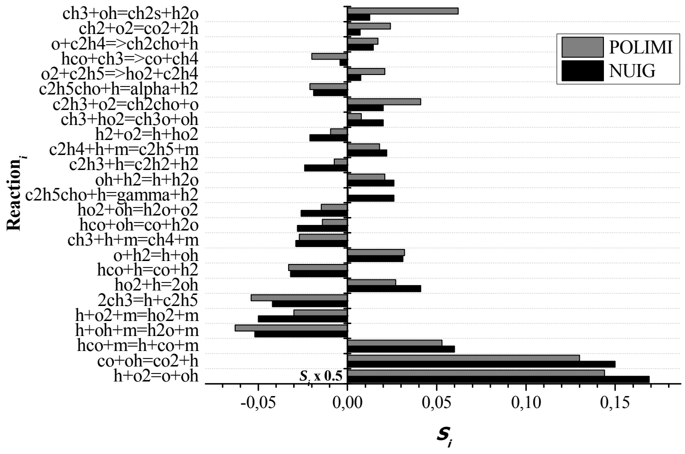

Figure 32: Sensitivity coefficients of laminar flame speed to rate constants for propanal/air flames at φ = 1.3, T_u = 343 K [48]. NUIG mechanism (black bars) and POLIMI mechanism (grey bars).

3.3.2 *n*-butanal

Experimental [49] and calculated laminar flame speeds for *n*-butanal/air mixtures at atmospheric pressure are reported in Figure 33. Both mechanisms are able to predict the measured values very well. Sensitivity analyses of flame speeds to rate constants have been carried out for both mechanisms at stoichiometric conditions, the results of which are reported in Figure 31. Again, the chemistry is mainly controlled by the C_0–C_4 sub-mechanism. In particular, apart from the highly sensitive reactions involving Ḣ, HĊO and ȮH, ethylene and vinyl radical oxidation chemistry controls the flame speed predictions.

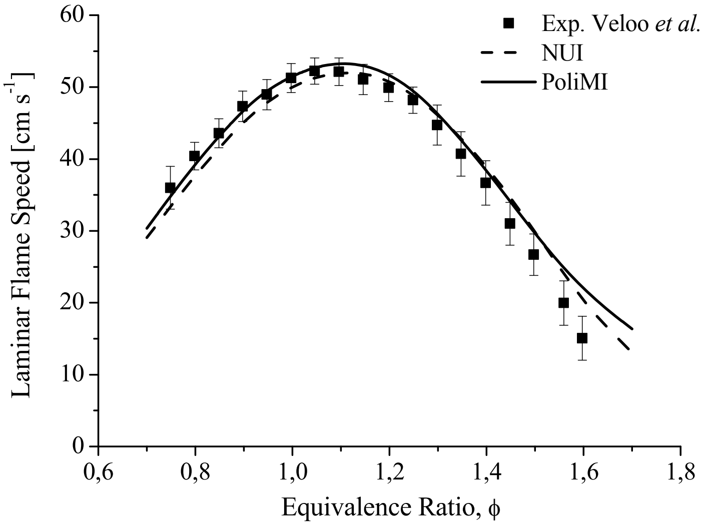

Figure 33: Experimental and computed laminar flame speeds of *n*-butanal/air flames at T_u = 343 K and p = 1 atm [49]. Experimental data (symbols) by Veloo et al. [49], POLIMI mechanism (solid lines) and NUIG mechanism (dashed lines).

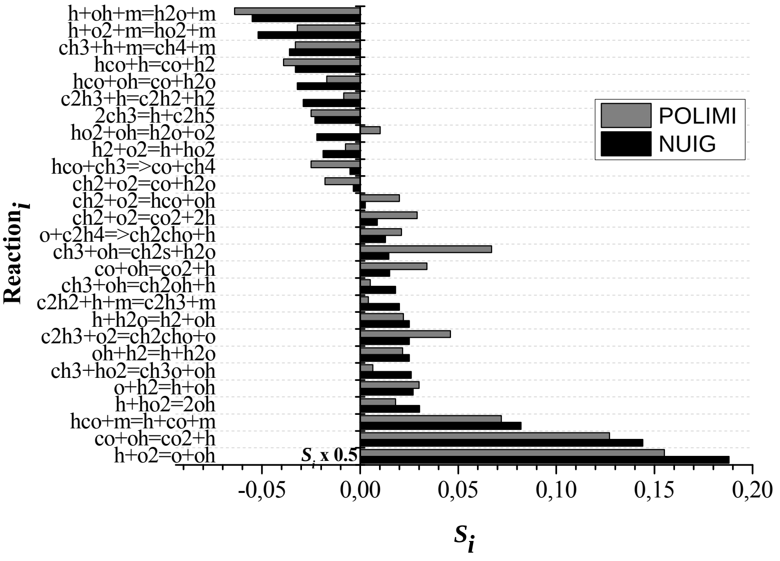

Figure 34: Sensitivity coefficients of laminar flame speed to rate constants for *n*-butanal/air flames at φ = 1.0 T_u = 343 K [49]. NUIG mechanism (black bars) and POLIMI mechanism (grey bars).

Include a comparison of C1-C5 aldehydes flame speed???

5 Conclusions

An experimental and kinetic modeling study of the high temperature pyrolysis and oxidation of C_3–C_5 *n*-aldehydes is presented in this work.

New experimental data have been provided for both pyrolysis and oxidation in shock tubes. Species profile measurements were carried out for the three aldehydes in a single pulse shock tube under pyrolytic conditions. Ignition delay times were measured for 1% fuel O_2/Ar mixtures at 1 and 3 atm in a UV emission shock tube for propanal, *n*-butanal and *n*-pentanal. In both oxidative and pyrolytic environment, propanal showed reactivity higher or at least comparable with that of *n*-pentanal, with *n*-butanal being the less reactive aldehyde.

For the first time the homologous series of C_3–C_5 has been analyzed in detail. Detailed mechanisms for the pyrolysis and oxidation of aldehydes was developed and discussed. The mechanism has been coupled with the C_0–C_4 kinetic mechanism of NUIG and of POLIMI. Both of the resulting mechanisms were then validated and compared with the complete set of experimental data.

Both mechanisms were able to closely reproduce the pyrolysis data, including major and minor species, within the experimental uncertainty. Ignition delay times were also satisfactorily captured by both mechanisms, with the NUIG mechanism being consistently slower than the POLIMI one. Experimental and calculated apparent activation energies of ignition delay times were also discussed, highlighting the large experimental variation of activation energies.

Laminar flame speeds of propanal and *n*-butanal were also quite satisfactorily compared with experimental measurements.

The validation of the aldehyde mechanism by coupling the primary reactions with the NUIG and POLIMI mechanisms further highlights the relevant role of the C_0–C_4 sub-mechanisms. The major differences between the models and the experiments can be attributed to the chemistry of the smaller species, more than to the specific fuel reactions. This observation further supports the need of an highly accurate C_0–C_4 sub-mechanism, which is well validated over as a wide a range of conditions possible as presented in previous work by Metcalfe *et al.* [59] and by Naik *et al.* [91].

References

1. Grosjean, D., *Formaldehyde and other carbonyls in Los Angeles ambient air.* Environmental Science & Technology, 1982. **16**(5): p. 254-262.
2. He, P.-J., et al., *The emission patterns of volatile organic compounds during aerobic biotreatment of municipal solid waste using continuous and intermittent aeration.* Journal of the Air & Waste Management Association, 2012. **62**(4): p. 461-470.
3. Grosjean, D., E. Grosjean, and A.W. Gertler, *On-Road Emissions of Carbonyls from Light-Duty and Heavy-Duty Vehicles.* Environmental Science & Technology, 2000. **35**(1): p. 45-53.
4. Zervas, E., *Regulated and non-regulated pollutants emitted from two aliphatic and a commercial diesel fuel.* Fuel, 2008. **87**(7): p. 1141-1147.
5. Karavalakis, G., S. Poulopoulos, and E. Zervas, *Impact of diesel fuels on the emissions of non-regulated pollutants.* Fuel, 2012. **102**(0): p. 85-91.
6. Abrantes, R.d., J.V.d. Assunção, and E.Y. Hirai, *Caracterização das emissões de aldeídos de veículos do ciclo diesel.* Revista de Saúde Pública, 2005. **39**: p. 479-485.
7. Roy, M.M., *HPLC analysis of aldehydes in automobile exhaust gas: Comparison of exhaust odor and irritation in different types of gasoline and diesel engines.* Energy Conversion and Management, 2008. **49**(5): p. 1111-1118.
8. Schauer, J.J., et al., *Measurement of Emissions from Air Pollution Sources. 5. C1−C32 Organic Compounds from Gasoline-Powered Motor Vehicles.* Environmental Science & Technology, 2002. **36**(6): p. 1169-1180.
9. Poulopoulos, S.G., D.P. Samaras, and C.J. Philippopoulos, *Regulated and unregulated emissions from an internal combustion engine operating on ethanol-containing fuels.* Atmospheric Environment, 2001. **35**(26): p. 4399-4406.
10. He, B.-Q., et al., *The effect of ethanol blended diesel fuels on emissions from a diesel engine.* Atmospheric Environment, 2003. **37**(35): p. 4965-4971.
11. Machado Corrêa, S. and G. Arbilla, *Carbonyl emissions in diesel and biodiesel exhaust.* Atmospheric Environment, 2008. **42**(4): p. 769-775.
12. Cahill, T.M. and R.A. Okamoto, *Emissions of Acrolein and Other Aldehydes from Biodiesel-Fueled Heavy-Duty Vehicles.* Environmental Science & Technology, 2012. **46**(15): p. 8382-8388.
13. Ballesteros, R., J.J. Hernández, and J. Guillén-Flores, *Carbonyls speciation in a typical European automotive diesel engine using bioethanol/butanol–diesel blends.* Fuel, 2012. **95**(0): p. 136-145.
14. Ranzi, E., et al., *Kinetic modeling of the thermal degradation and combustion of biomass.* Chemical Engineering Science, (0).
15. Frassoldati, A., et al., *An experimental and kinetic modeling study of n-propanol and iso-propanol combustion.* Combustion and Flame, 2010. **157**(1): p. 2-16.
16. Togbé, C., et al., *2-Propanol Oxidation in a Pressurized Jet-Stirred Reactor (JSR) and Combustion Bomb: Experimental and Detailed Kinetic Modeling Study.* Energy & Fuels, 2011. **25**(2): p. 676-683.
17. Galmiche, B., et al., *Experimental and Detailed Kinetic Modeling Study of the Oxidation of 1-Propanol in a Pressurized Jet-Stirred Reactor (JSR) and a Combustion Bomb.* Energy & Fuels, 2011. **25**(5): p. 2013-2021.
18. Man, X., et al., *An experimental and kinetic modeling study of n-propanol and i-propanol ignition at high temperatures.* Combustion and Flame, (0).
19. Black, G., et al., *Bio-butanol: Combustion properties and detailed chemical kinetic model.* Combustion and Flame, 2010. **157**(2): p. 363-373.
20. Sarathy, S.M., et al., *An experimental and kinetic modeling study of n-butanol combustion.* Combustion and Flame, 2009. **156**(4): p. 852-864.
21. Sarathy, S.M., et al., *A comprehensive chemical kinetic combustion model for the four butanol isomers.* Combustion and Flame, 2012. **159**(6): p. 2028-2055.
22. Grana, R., et al., *An experimental and kinetic modeling study of combustion of isomers of butanol.* Combustion and Flame, 2010. **157**(11): p. 2137-2154.

23. Frassoldati, A., et al., *Detailed kinetic modeling of the combustion of the four butanol isomers in premixed low-pressure flames.* Combustion and Flame, 2012. **159**(7): p. 2295-2311.
24. Vasu, S.S. and S.M. Sarathy, *On the High-Temperature Combustion of n-Butanol: Shock Tube Data and an Improved Kinetic Model.* Energy & Fuels, 2013. **27**(11): p. 7072-7080.
25. Togbé, C., et al., *Experimental and detailed kinetic modeling study of 1-pentanol oxidation in a JSR and combustion in a bomb.* Proceedings of the Combustion Institute, 2011. **33**(1): p. 367-374.
26. Mani Sarathy, S., et al., *A comprehensive experimental and modeling study of iso-pentanol combustion.* Combustion and Flame, 2013. **160**(12): p. 2712-2728.
27. Heufer, K.A., et al., *Detailed Kinetic Modeling Study of n-Pentanol Oxidation.* Energy & Fuels, 2012. **26**(11): p. 6678-6685.
28. Yasunaga, K., et al., *A shock tube and chemical kinetic modeling study of the pyrolysis and oxidation of butanols.* Combustion and Flame, 2012. **159**(6): p. 2009-2027.
29. Dean, A.M., R.L. Johnson, and D.C. Steiner, *Shock-tube studies of formaldehyde oxidation.* Combustion and Flame, 1980. **37**(0): p. 41-62.
30. Hochgreb, S. and F.L. Dryer, *A comprehensive study on CH2O oxidation kinetics.* Combustion and Flame, 1992. **91**(3–4): p. 257-284.
31. Li, J., et al., *A comprehensive kinetic mechanism for CO, CH2O, and CH3OH combustion.* International Journal of Chemical Kinetics, 2007. **39**(3): p. 109-136.
32. Friedrichs, G., D.F. Davidson, and R.K. Hanson, *Direct measurements of the reaction H + CH2O → H2 + HCO behind shock waves by means of Vis–UV detection of formaldehyde.* International Journal of Chemical Kinetics, 2002. **34**(6): p. 374-386.
33. Eiteneer, B., et al., *Determination of Rate Coefficients for Reactions of Formaldehyde Pyrolysis and Oxidation in the Gas Phase.* The Journal of Physical Chemistry A, 1998. **102**(27): p. 5196-5205.
34. Hidaka, Y., et al., *Shock-tube study of CH2O pyrolysis and oxidation.* Combustion and Flame, 1993. **92**(4): p. 365-376.
35. Glarborg, P., et al., *Oxidation of formaldehyde and its interaction with nitric oxide in a flow reactor.* Combustion and Flame, 2003. **132**(4): p. 629-638.
36. Halstead, M.P., A. Prothero, and C.P. Quinn, *A Mathematical Model of the Cool-Flame Oxidation of Acetaldehyde.* Proceedings of the Royal Society of London. A. Mathematical and Physical Sciences, 1971. **322**(1550): p. 377-403.
37. Gray, P., et al., *Oscillatory Ignitions and Cool Flames Accompanying the Non-Isothermal Oxidation of Acetaldehyde in a Well Stirred, Flow Reactor.* Proceedings of the Royal Society of London. A. Mathematical and Physical Sciences, 1981. **374**(1758): p. 313-339.
38. Cavanagh, J., R.A. Cox, and G. Olson, *Computer modeling of cool flames and ignition of acetaldehyde.* Combustion and Flame, 1990. **82**(1): p. 15-39.
39. Di Maio, F.P., P.G. Lignola, and P. Talarico, *Thermokinetic Oscillations in Acetaldehyde CSTR Combustion.* Combustion Science and Technology, 1993. **91**(1-3): p. 119-142.
40. Kaiser, E.W., C.K. Westbrook, and W.J. Pitz, *Acetaldehyde oxidation in the negative temperature coefficient regime: Experimental and modeling results.* International Journal of Chemical Kinetics, 1986. **18**(6): p. 655-688.
41. Dagaut, P., et al., *Acetaldehyde Oxidation in a JSR and Ignition in Shock Waves: Experimental and Comprehensive Kinetic Modeling.* Combustion Science and Technology, 1995. **107**(4-6): p. 301-316.
42. Hidaka, Y., et al., *Shock-tube study of acetaldehyde pyrolysis*, in *Shock Waves*, Z. Jiang, Editor 2005, Springer Berlin Heidelberg. p. 603-608.
43. Yasunaga, K., et al., *Shock-tube and modeling study of acetaldehyde pyrolysis and oxidation.* International Journal of Chemical Kinetics, 2008. **40**(2): p. 73-102.
44. Kaiser, E.W., *A modeling study of the oxidation of propionaldehyde in the negative temperature coefficient regime.* International Journal of Chemical Kinetics, 1987. **19**(5): p. 457-486.
45. Lifshitz, A., C. Tamburu, and A. Suslensky, *Decomposition of propanal at elevated temperatures: experimental and modeling study.* The Journal of Physical Chemistry, 1990. **94**(7): p. 2966-2972.
46. Kasper, T., et al., *Structure of a stoichiometric propanal flame at low pressure.* Proceedings of the Combustion Institute, 2009. **32**(1): p. 1285-1292.

47. Akih-Kumgeh, B. and J.M. Bergthorson, *Ignition of C3 oxygenated hydrocarbons and chemical kinetic modeling of propanal oxidation.* Combustion and Flame, 2011. **158**(10): p. 1877-1889.
48. Veloo, P.S., et al., *Jet-stirred reactor and flame studies of propanal oxidation.* Proceedings of the Combustion Institute, 2013. **34**(1): p. 599-606.
49. Veloo, P.S., et al., *Experimental and modeling study of the oxidation of n- and iso-butanal.* Combustion and Flame, 2013. **160**(9): p. 1609-1626.
50. Davidson, D., et al., *Ignition delay time measurements of normal alkanes and simple oxygenates.* Journal of Propulsion and Power, 2010. **26**(2): p. 280-287.
51. Dooley, S., H.J. Curran, and J.M. Simmie, *Autoignition measurements and a validated kinetic model for the biodiesel surrogate, methyl butanoate.* Combustion and Flame, 2008. **153**(1–2): p. 2-32.
52. Zhang, J., et al., *A shock tube and kinetic modeling study of n-butanal oxidation.* Combustion and Flame, 2013. **160**(9): p. 1541-1549.
53. Zhang, J., et al., *Shock Tube and Kinetic Modeling Study of Isobutanal Oxidation.* Energy & Fuels, 2013. **27**(5): p. 2804-2810.
54. da Silva, G. and J.W. Bozzelli, *Enthalpies of Formation, Bond Dissociation Energies, and Molecular Structures of the n-Aldehydes (Acetaldehyde, Propanal, Butanal, Pentanal, Hexanal, and Heptanal) and Their Radicals.* The Journal of Physical Chemistry A, 2006. **110**(48): p. 13058-13067.
55. Healy, D., et al., *< i> n</i>-Butane: Ignition delay measurements at high pressure and detailed chemical kinetic simulations.* Combustion and Flame, 2010. **157**(8): p. 1526-1539.
56. Healy, D., et al., *Oxidation of C1−C5 Alkane Quinternary Natural Gas Mixtures at High Pressures.* Energy & Fuels, 2010. **24**(3): p. 1521-1528.
57. Healy, D., et al., *Methane/n-Butane Ignition Delay Measurements at High Pressure and Detailed Chemical Kinetic Simulations.* Energy & Fuels, 2010. **24**(3): p. 1617-1627.
58. Burke, S., *Development of a Chemical Kinetic Mechanism for Small Hydrocarbons*, in *Ph.D. Thesis*2013, National University of Ireland Galway. p. 340.
59. Metcalfe, W.K., et al., *A Hierarchical and Comparative Kinetic Modeling Study of C1 − C2 Hydrocarbon and Oxygenated Fuels.* International Journal of Chemical Kinetics, 2013. **45**(10): p. 638-675.
60. Kéromnès, A., et al., *An experimental and detailed chemical kinetic modeling study of hydrogen and syngas mixture oxidation at elevated pressures.* Combustion and Flame, 2013. **160**(6): p. 995-1011.
61. Ranzi, E., et al., *Hierarchical and comparative kinetic modeling of laminar flame speeds of hydrocarbon and oxygenated fuels.* Progress in Energy and Combustion Science, 2012. **38**(4): p. 468-501.
62. Hidaka, Y., et al., *Thermal decomposition of ethane in shock waves.* International Journal of Chemical Kinetics, 1985. **17**(4): p. 441-453.
63. Hidaka, Y., et al., *Thermal decomposition of propyne and allene in shock waves.* International Journal of Chemical Kinetics, 1989. **21**(8): p. 643-666.
64. Hidaka, Y., et al., *Shock-tube and modeling study of acetylene pyrolysis and oxidation.* Combustion and Flame, 1996. **107**(4): p. 401-417.
65. Hidaka, Y., et al., *Shock tube and modeling study of ketene oxidation.* Combustion and Flame, 1996. **106**(1–2): p. 155-167.
66. Smith, J.M., J.M. Simmie, and H.J. Curran, *Autoignition of heptanes; experiments and modeling.* International Journal of Chemical Kinetics, 2005. **37**(12): p. 728-736.
67. Morley, C. *Gaseq*. Jan 2005 [cited 2012; Available from: http://www.gaseq.co.uk.
68. Ritter, E.R. and J.W. Bozzelli, *THERM: Thermodynamic property estimation for gas phase radicals and molecules.* International Journal of Chemical Kinetics, 1991. **23**(9): p. 767-778.
69. Benson, S.W., *Thermochemical kinetics: methods for the estimation of thermochemical data and rate parameters*1976: Wiley New York.
70. Dean, A.M., *Predictions of pressure and temperature effects upon radical addition and recombination reactions.* The Journal of Physical Chemistry, 1985. **89**(21): p. 4600-4608.

71. Chang, A., J. Bozzelli, and A. Dean, *Kinetic analysis of complex chemical activation and unimolecular dissociation reactions using QRRK theory and the modified strong collision approximation.* Zeitschrift für Physikalische Chemie, 2000. **214**(11/2000): p. 1533.
72. Kassel, L.S., *Studies in Homogeneous Gas Reactions. I.* The Journal of Physical Chemistry, 1928. **32**(2): p. 225-242.
73. Serinyel, Z., et al., *Experimental and Chemical Kinetic Modeling Study of 3-Pentanone Oxidation.* The Journal of Physical Chemistry A, 2010. **114**(46): p. 12176-12186.
74. Simmie, J.M., *Kinetics and Thermochemistry of 2,5-Dimethyltetrahydrofuran and Related Oxolanes: Next Next-Generation Biofuels.* The Journal of Physical Chemistry A, 2012. **116**(18): p. 4528-4538.
75. Curran, H.J., *Rate constant estimation for C1 to C4 alkyl and alkoxyl radical decomposition.* International Journal of Chemical Kinetics, 2006. **38**(4): p. 250-275.
76. Huynh, L.K. and A. Violi. *Ab Initio Study on the Methyl Butanoate Decomposition*. in *The 2007 Annual Meeting*. 2007.
77. Orme, J.P., H.J. Curran, and J.M. Simmie, *Experimental and Modeling Study of Methyl Cyclohexane Pyrolysis and Oxidation.* The Journal of Physical Chemistry A, 2005. **110**(1): p. 114-131.
78. Matheu, D.M., W.H. Green, and J.M. Grenda, *Capturing pressure-dependence in automated mechanism generation: Reactions through cycloalkyl intermediates.* International Journal of Chemical Kinetics, 2003. **35**(3): p. 95-119.
79. Dente, M., et al., *Kinetic Modelling of Pyrolysis Processes in Gas and Condensed Phase*, in *Advances in Chemical Engineering*, B.M. Guy, Editor 2007, Academic Press. p. 51-166.
80. Curran, H.J., et al., *A Comprehensive Modeling Study of n-Heptane Oxidation.* Combustion and Flame, 1998. **114**(1–2): p. 149-177.
81. Cuoci, A., et al. *Open SMOKE: numerical modeling of reacting systems with detailed kinetic mechanisms*. in *XXXIV meeting of the Italian Section of the Combustion Institute*. 2011.
82. Manca, D., et al., *Numerical problems in the solution of oxidation and combustion models.* Combustion Theory and Modelling, 2001. **5**(2): p. 185-199.
83. Buzzi-Ferraris, G. and F. Manenti, *BzzMath: Library Overview and Recent Advances in Numerical Methods.* Computer Aided Chemical Engineering, 2012. **30**(2): p. 1312-1316.
84. William H. Green, J.W.A., Beat A. Buesser, Robert W. Ashcraft, Gregory J. Beran, Caleb A. Class, Connie Gao, C. Franklin Goldsmith, Michael R. Harper, Amrit Jalan, Murat Keceli, Gregory R. Magoon, David M. Matheu, Shamel S. Merchant, Jeffrey D. Mo, Sarah Petway, Sumathy Raman, Sandeep Sharma, Jing Song, Yury Suleymanov, Kevin M. Van Geem, John Wen, Richard H. West, Andrew Wong, Hsi-Wu Wong, Paul E. Yelvington, Nathan Yee, Joanna Yu. *"RMG - Reaction Mechanism Generator v4.0.1"*. 2013; Available from: http://rmg.sourceforge.net.
85. Zhou, C.-W., J.M. Simmie, and H.J. Curran, *Ab initio and kinetic study of the reaction of ketones with $\dot{\mathrm{O}}$H for T= 500–2000 K. Part I: hydrogen-abstraction from H3CC (O) CH3–x (CH3) x, x= 0↦2.* Physical Chemistry Chemical Physics, 2011. **13**(23): p. 11175-11192.
86. Mendes, J., C.-W. Zhou, and H.J. Curran, *Theoretical and Kinetic Study of the Reactions of Ketones with H$\dot{\mathrm{O}}$2 Radicals. Part I: Abstraction Reaction Channels.* The Journal of Physical Chemistry A, 2013. **117**(22): p. 4515-4525.
87. Ranzi, E., et al., *Prediction of Kinetic Parameters for Hydrogen Abstraction Reactions.* Combustion Science and Technology, 1993. **95**(1-6): p. 1-50.
88. Ranzi, E., et al., *Lumping procedures in detailed kinetic modeling of gasification, pyrolysis, partial oxidation and combustion of hydrocarbon mixtures.* Progress in Energy and Combustion Science, 2001. **27**(1): p. 99-139.
89. Kee, R.J., F.M. Rupley, and J.A. Miller, *Chemkin-II: A Fortran chemical kinetics package for the analysis of gas-phase chemical kinetics*, 1989, Sandia National Labs., Livermore, CA (USA).
90. Burcat, A., et al., *Third millenium ideal gas and condensed phase thermochemical database for combustion (with update from active thermochemical tables)*, 2005. p. Medium: ED.

91. Naik, C.V., K.V. Puduppakkam, and E. Meeks, *An Improved Core Reaction Mechanism for Saturated C0-C4 Fuels.* Journal of engineering for gas turbines and power, 2012. **134**(2).

Figure 1: a) Oxidation of formaldehyde at 1 atm and 1095 K [31]. b) Pyrolysis of acetaldehyde at 2 atm and 2 ms residence time [43]. Comparison of experimental data (symbols) and predictions of NUIG (dashed lines) and POLIMI (solid lines) kinetic schemes. 4
Figure 2: Ignition delay times of formaldehyde [34] and acetaldehyde [43] oxidation. Comparison of experimental data (symbols) and predictions of NUIG (dashed lines) and POLIMI (solid lines) kinetic schemes. 5
Figure 3: End-wall pressure trace and CH^* chemiluminescence measurements with corresponding ignition delay time, *n*-butanal 1%, O_2 5.5%, Ar 93.5%, p = 1.2 atm, T = 1349.1 K.......... 7
Figure 4: propanal, *n*-butanal and *n*-pentanal chemical structure and named carbon sites 8
Figure 5: Primary decomposition reactions of propanal.......... 9
Figure 6: Primary decomposition reactions of *n*-butanal 9
Figure 7: Primary decomposition reactions of *n*-pentanal.......... 10
Figure 8: Isomerization (solid lines) and decomposition (dashed lines) reactions of *n*-pentanal ε-radical (a), δ-radical (b), γ-radical (c), β-radical (d). 14
Figure 9: Predicted and experimental concentration profiles from shock tube pyrolysis of 1% propanal in argon [45]. Experimental (symbols), POLIMI mechanism (solid lines) and NUIG mechanism (dashed lines). 17
Figure 10: Predicted and experimental concentration profiles from shock tube pyrolysis of 3% *n*-butanal in argon. Experiments (symbols), POLIMI mechanism (solid lines) and NUIG mechanism (dashed lines)...... 18
Figure 11: Predicted and experimental concentration profiles from shock tube pyrolysis of 3% *n*-butanal in argon. Experiments (symbols), POLIMI mechanism (solid lines) and NUIG mechanism (dashed lines)...... 19
Figure 12: Global rate of production analysis carried out at 1200 K under the pyrolysis conditions studied as part of this work, NUIG mechanism (bold) and POLIMI mechanism (standard). 19
Figure 13: Predicted and experimental concentration profiles from shock tube pyrolysis of 3% *n*-pentanal in argon. Experiments (symbols), POLIMI mechanism (solid lines) and NUIG mechanism (dashed lines)...... 20
Figure 14: Fuel concentration profiles from shock tube pyrolysis (3% in argon), experiments from this work (a), POLIMI mechanism (b) and NUIG mechanism (c) predictions. 20
Figure 15: Predicted and experimental ignition delay times of 1% propanal in O_2/Ar mixtures. Experiments (symbols), POLIMI mechanism (solid lines) and NUIG mechanism (dashed lines). 21
Figure 16:Predicted and experimental ignition delay times of O_2/Ar mixtures containing 1.25% propanal [47]. Experiments (symbols), POLIMI mechanism (solid lines) and NUIG mechanism (dashed lines). 22
Figure 17: Rate of production analysis for 1% propanal in O_2/Ar mixtures at φ = 1.0, p = 1atm. NUIG mechanism, T = 1150 K (italic) and 1620 K (bold).......... 22
Figure 18: Sensitivity coefficients of ignition delay times to rate constants for 1% propanal in O_2/Ar mixtures at φ=1.0, p=1atm, 1150 K (black bars) and 1620 K (grey bars). NUIG mechanism.......... 23
Figure 19: Predicted and experimental ignition delay times of O_2/Ar mixtures containing 1 % *n*-butanal. Experiments (symbols), POLIMI mechanism (solid lines) and NUIG mechanism (dashed lines). 24

Figure 20: Predicted and experimental ignition delay times of O_2/Ar mixtures containing 1 % *n*-butanal [50]. Experiments (symbols), POLIMI mechanism (solid lines) and NUIG mechanism (dashed lines). 24
Figure 21: Comparison amongst experimental ignition delay times for *n*-butanal-O_2/Ar mixtures, scaled at 1.7 atm. This work: 1% fuel at 1 atm (squares); Zhang et al [52]: 1.2% fuel at 1.3 atm (triangles); Davidson *et al*. (circles) [50]: 1% fuel at 1.7 atm. 25
Figure 22: Predicted and experimental ignition delay times of *n*-butanal in O_2/Ar mixtures [52]. Experiments (symbols), POLIMI mechanism (solid lines) and NUIG mechanism (dashed lines). 25
Figure 23: Rate of production analysis for 1% *n*-butanal in O_2/Ar mixtures at p = 3atm, T = 1320 K at $\varphi = 0.5$ (bold) and $\varphi = 2.0$ (standard). 26
Figure 24: Sensitivity coefficients of ignition delay times to rate constants for 1% *n*-butanal in O_2/Ar mixtures at p = 3 atm, T = 1320 K at $\varphi = 0.5$ (black bars) and $\Phi = 2.0$ (grey bars). 26
Figure 25: Predicted and experimental ignition delay times of O_2/Ar mixtures containing 1% *n*-pentanal. Experiments (symbols), POLIMI mechanism (solid lines) and NUIG mechanism (dashed lines). 27
Figure 26: Rate of production analysis for 1% *n*-pentanal in O_2/Ar mixtures at $\varphi = 1.0$, p = 2 atm, T = 1300 K, POLIMI mechanism. 27
Figure 27: Sensitivity coefficients of ignition delay times to rate constants for 1% n-pentanal in O_2/Ar mixtures at $\varphi = 1.0$, p = 2 atm, T = 1300 K. NUIG mechanism (black bars), POLIMI mechanism (grey bars). 28
Figure 28: 1% fuel–O_2/Ar mixtures; $\varphi = 0.5$, p = 1 atm, experimental data from present work (symbols) and linear fit (lines). 28
Figure 29: 1% fuel-O_2/Ar mixtures, experimental apparent activation energies E_a at 1 and 3 atm pressure. 29
Figure 30: fuel-O_2/Ar mixtures, experimental apparent activation energies E_a. 29
Figure 31: Experimental and computed laminar flame speeds of propanal/air flames at T_u = 343 K and p = 1 atm. Experimental data (symbols) by Veloo et al.[48], POLIMI mechanism (solid lines) and NUIG mechanism (dashed lines). 30
Figure 32: Sensitivity coefficients of laminar flame speed to rate constants for propanal/air flames at $\varphi = 1.3$, T_u = 343 K [48]. NUIG mechanism (black bars) and POLIMI mechanism (grey bars). 31
Figure 33: Experimental and computed laminar flame speeds of *n*-butanal/air flames at T_u = 343 K and p = 1 atm [49]. Experimental data (symbols) by Veloo et al. [49], POLIMI mechanism (solid lines) and NUIG mechanism (dashed lines). 31
Figure 34: Sensitivity coefficients of laminar flame speed to rate constants for *n*-butanal/air flames at $\varphi = 1.0$ T_u = 343 K [49]. NUIG mechanism (black bars) and POLIMI mechanism (grey bars). 32

Table 1: Summary of experimental work carried out in the SPST at the National Defense Academy, Japan. 5
Table 2: Summary of experimental work carried out in the low pressure shock tube at the National University of Ireland, Galway. 7
Table 3: Thermochemical data and nomenclature of aldehydes and related primary radicals (*group additivity). 8
Table 4: Calculated Bond Dissociation Energies (kcal mol^{-1}) of C–C and C–H bonds and comparison to ab initio computed values by da Silva and Bozzelli [54] 10
Table 5: Rate parameters of initiation reactions and relative branching ratios at different temperatures 11
Table 6: Rate parameters of decomposition and isomerization reactions of aldehyde radicals [units are: cm3, mol, s, cal] and references (* extended analogy as discussed in this paper). 13

Supplementary material

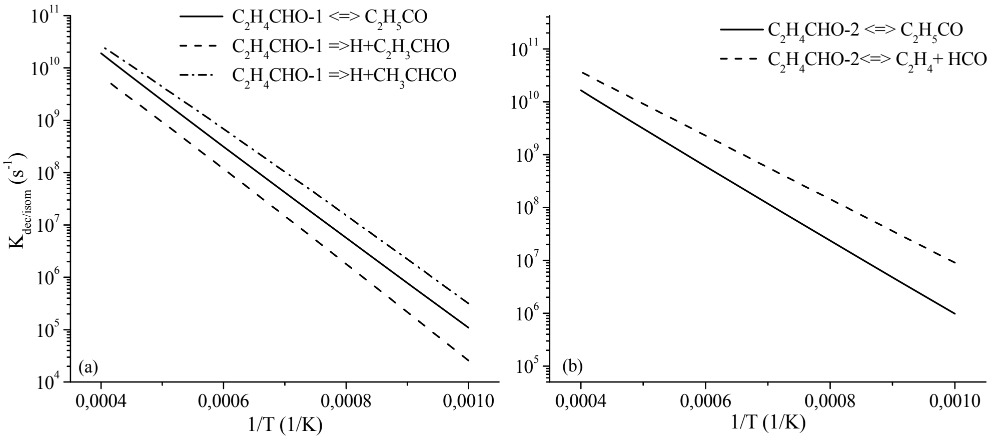

Isomerization (solid lines) and decomposition (dashed lines) reactions rate constant of propanal radicals.

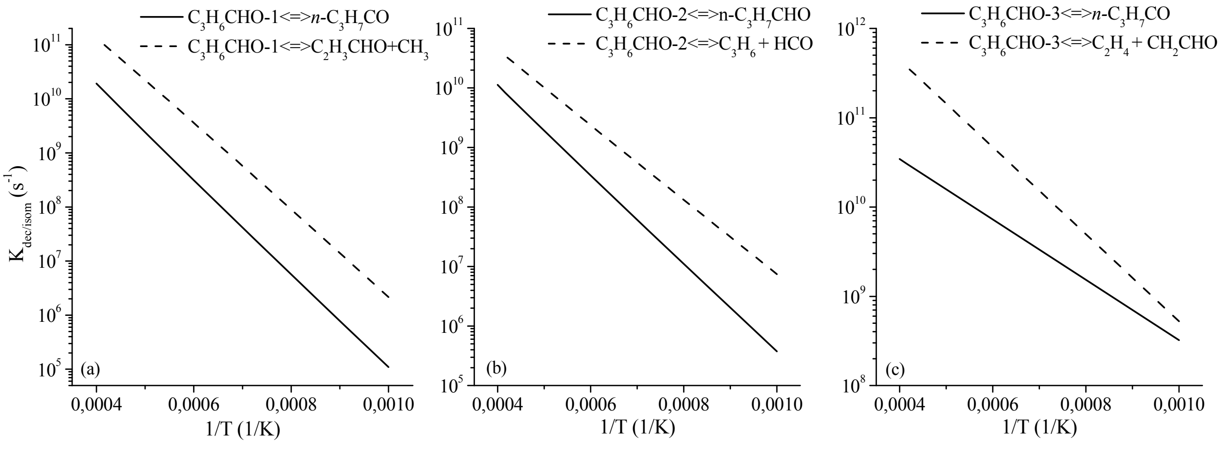

Isomerization (solid lines) and decomposition (dashed lines) reactions rate constant of *n*-butanal radicals.

Aldehyde	***Reactor/Facility***		***T [K]***	***P [atm]***	**Φ**	***Ref***
Formaldehyde	Shock Tube	Pyrolysis	1160–1890	1.4–2.5	/	Hidaka et al. (1993a)
	"	"	1200–2000	1.3–3.0	/	Hidaka et al. (1993b)
	"	"	1560–2276	0.9–2.5	/	Eiteneer et al. (1998)
	"	Oxidation	1600–3000	1.0–2.0	0.54, 0.63	Dean et al. (1980)
	"	"	1160–1618	1.4–2.5	0.25, 0.5, 1.0, 2.0, 4.0	Hidaka et al. (1993b)
	"	"	1334–1974	0.8–2.3	0.16, 0.25, 1.0, 1.7, 5.9	Eiteneer et al. (1998)
	Plug Flow Reactor	"	945	1.0	1.56	Li et al. (2007)
	"	"	1095	1.0	0.93	"
Acetaldehyde	Shock Tube	Pyrolysis	1013–1577	1.2–2.8	/	Yasunaga et al. (2008)
	Jet Stirred Reactor	Oxidation	900–1300	1,10	0.09, 0.43, 0.82, 1.0, 1.61	Dagaut et al. (1995)
	Shock Tube	"	1276–1703	1.7–2.6	0.2, 0.4, 1	Yasunaga et al. (2008)
Propanal	Shock Tube	Pyrolysis	970–1300	2.0–2.7	/	Lifshitz et al. (1990)
	"	"	972–1372	1.4–2.8	/	**This work**
	"	Oxidation	1170–1750	1.0, 3.0	0.5, 1.0, 2.0	**This work**
	"	"	1150–1560	1.0, 12.0	0.5, 1.0	Akih-Kumgeh (2011)
	Premixed Flat Flame	"	314–2000	0.05	1.0	Kasper et al. (2009)
	Laminar Premixed Flames	"	343–2320	1.0	0.75-1.6	Veloo et al. (2013)
n-butanal	Shock Tube	Pyrolysis	1096–1368	1.1–2.8	/	**This work**
	"	Oxidation	1190–1550	1.7	1.0, 2.0	Davidson et al. (2010)
	"	"	1180–1580	1.3, 5, 10	0.5, 1.0, 2.0	Zhang et al. (2013)
	"	"	1224–1634	1.0, 3.0	0.5, 1.0, 2.0	**This work**
	Laminar Premixed Flames	"	343–2320	1.0	0.75-1.6	Veloo et al. (2013)
n-pentanal	Shock Tube	Pyrolysis	970–1370	1.4–2.8	/	**This work**
	"	Oxidation	1090–1850	1.0, 3.0	0.5, 1.0, 2.0	**This work**

Aldehyde			***H·***			***OH·***		
	site	***type***	***A [cm3/s/mol]***	***n***	***Ea [kcal/mol]***	***A [cm3/s/mol]***	***n***	***Ea [kcal/mol]***
formaldehyde	α	a	4.50E+14	0.0	7500.	3.20E+06	2.0	–2066.
acetaldehyde	α	a	4.50E+14	0.0	7500.	2.30E+06	2.0	–1735.
	β	p	7.22E+06	2.0	6675.	1.20E+06	2.0	611.
propanal	α	a	2.00E+14	0.0	6362.	7.60E+12	0.0	630.
	β	s'	7.22E+06	2.0	3951.	9.60E+05	2.0	–2260.
	γ	p	7.22E+06	2.0	6526.	1.20E+06	2.0	–474.
n-butanal	α	a	2.00E+14	0.0	6360.	1.00E+06	2.0	–3344.
	β	s'	7.22E+06	2.0	3951.	9.60E+05	2.0	–2260.
	γ	s	4.81E+06	2.0	3951.	7.99E+05	2.0	–2260.
	δ	p	7.22E+06	2.0	6526.	1.20E+06	2.0	–474.
n-pentanal	α	a	2.00E+14	0.0	6360.	1.00E+06	2.0	–3344.
	β	s'	7.50E+13	0.0	7925.	7.10E+12	0.0	1715.
	γ	s	1.25E+14	0.0	7925.	7.99E+05	2.0	–2260.
	δ	s	1.25E+14	0.0	7925.	7.99E+05	2.0	–2260.
	ε	p	7.22E+06	2.0	6526.	1.20E+06	2.0	–474.

H-abstraction by H and OH rate parameters, POLIMI mechanism. a=acyl, p=primary, s’=resonantly stabilized secondary, s=secondary

Aldehyde			***H·***			***OH·***		
	site	***type***	***A [cm3/s/mol]***	***n***	***Ea [kcal/mol]***	***A [cm3/s/mol]***	***n***	***Ea [kcal/mol]***
formaldehyde	α	a	5.74E+07	1.90	2740.	7.82E+07	1.63	–1055.
acetaldehyde	α	a	1.31E+05	2.58	1220.	3.37E+12	0.00	–619.
	β	p	2.72E+03	3.10	5210.	1.72E+05	2.40	815.
propanal	α	a	1.00E+05	2.58	1220.	1.70E+12	0.00	–619.
	β	s'	2.15E+06	2.29	2880.	2.36E+02	3.15	3050.
	γ	p	3.50E+05	2.69	6450.	5.28E+09	0.97	1590.
n-butanal	α	a	1.00E+05	2.58	1220.	1.70E+12	0.00	–619.
	β	s'	2.15E+06	2.29	2880.	2.36E+02	3.15	3050.
	γ	s	1.30E+06	2.4	4471.	4.67E+07	1.61	–35.
	δ	p	2.63E+05	2.69	6450.	2.64E+09	0.97	1590.
n-pentanal	α	a	1.00E+05	2.58	1220.	1.70E+12	0.00	–619.
	β	s'	2.15E+06	2.29	2880.	2.36E+02	3.15	3050.
	γ	s	1.30E+06	2.40	4471.	4.67E+07	1.61	–35.
	δ	s	1.30E+06	2.40	4471.	4.67E+07	1.61	–35.
	ε	p	2.63E+05	2.69	6450.	2.64E+09	0.97	1590.

H-abstraction by H and OH rate parameters, NUIG mechanism. a=acyl, p=primary, s’=resonantly stabilized secondary, s=secondary

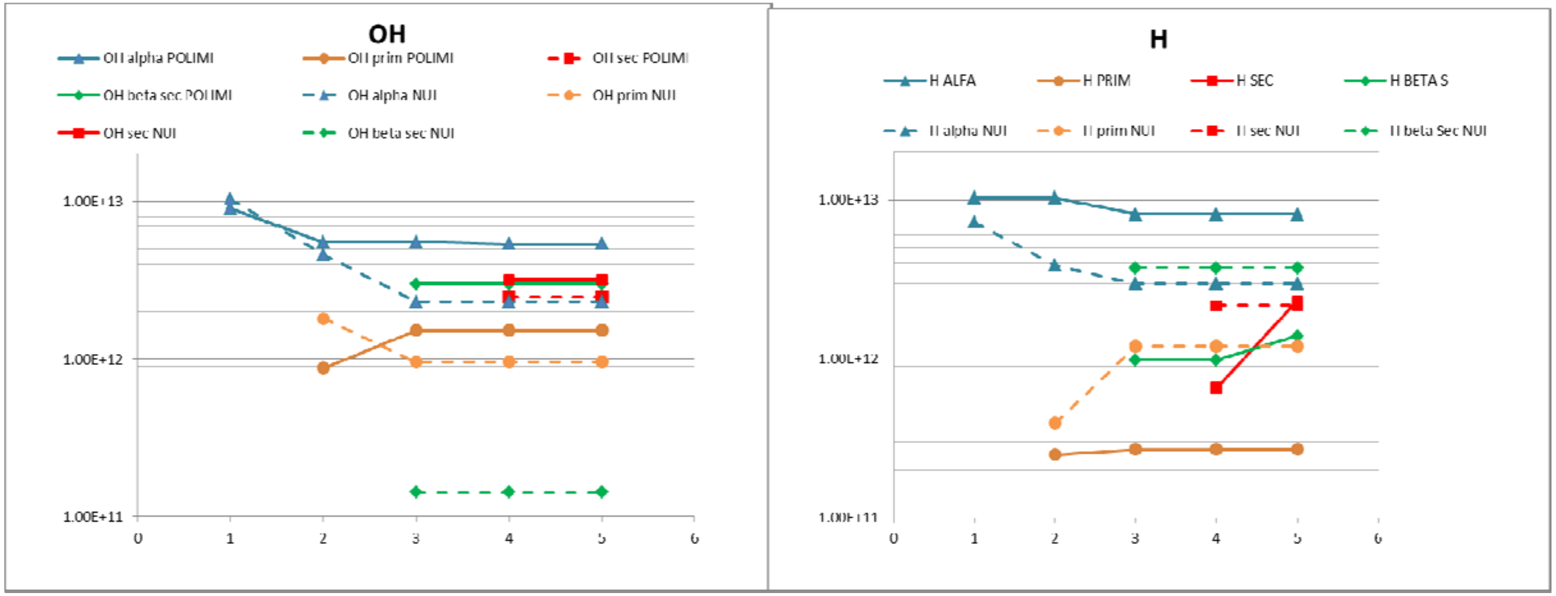

H-abstraction rate constant comparison (*T*=1000 K), NUIG (dashed), POLIMI (solid) mechanisms.

[ref]	***p* [atm]**	**Φ**	**$E_{a\ EXP}$ [kcal mol^{-1}]**	**$E_{a\ NUIG}$ [kcal mol^{-1}]**	**$E_{a\ PoliMI}$ [kcal mol^{-1}]**
		propanal			
This work	1	0.5	27.6	38.6	48.5
	1	1	23.2	34.8	38.5
	1	2	27.0	31.7	35.3
	3	0.5	36.1	38.6	44.0
	3	1	41.8	36.8	39.2
	3	2	30.2	35.4	37.8
Akih-Kumgeh et al. [47]	1	0.5	25.4	37.0	44.4
	1	1	23.6	34.8	39.0
	12	0.5	27.0	31.2	32.6
	12	1	31.4	30.9	29.9
		***n*-butanal**			
This work	*1*	*0.5*	35.9	44.9	52.9
	1	*1*	37.1	41.5	49.1
	1	*2*	35.1	37.7	40.5
	3	*0.5*	44.3	45.6	49.9
	3	*1*	39.7	44.6	51.7
	3	*2*	34.6	41.0	46.2
Zhang et al. [52]	*1.3*	*0.5*	43.3	40.3	47.3
	1.3	*1*	39.4	43.2	46.0
	1.3	*2*	35.2	39.0	45.1
	5	*0.5*	44.7	44.7	48.9
	5	*1*	44.1	45.3	52.3
	5	*2*	36.8	44.1	46.3
	10	*0.5*	41.7	42.5	40.1
	10	*1*	40.9	45.2	46.4
	10	*2*	37.0	44.1	45.3
Davidson et al. [50]	*1.7*	*1*	44.3	44.5	52.8
	1.7	*2*	40.4	39.5	44.4
		***n*-pentanal**			
This work	*1*	*0.5*	36.9	41.4	47.8
	1	*1*	34.1	39.2	39.3
	1	*2*	29.3	35.3	39.9
	3	*0.5*	26.3	36.7	41.7
	3	*1*	32.1	38.9	37.4
	3	*2*	28.3	36.3	34.5